



HI 21 cm observation and mass models of the extremely thin galaxy FGC 1440

K. Aditya¹ *, Peter Kamphuis², Arunima Banerjee¹  †, Sviatoslav Borisov^{3,4,5}
Aleksandr Mosenkov⁶, Aleksandra Antipova⁵, Dmitry Makarov⁵

¹ Department of Physics, Indian Institute of Science Education and Research (IISER) Tirupati, Tirupati - 517507, India

² Ruhr Universität Bochum, Astronomisches Institut, Universitätsstrasse 150, D-44801 Bochum, Germany

³ Department of Astronomy, University of Geneva, Chemin Pegasi 51, 1290 Versoix, Switzerland

⁴ Sternberg Astronomical Institute, M.V. Lomonosov Moscow State University, Universitetsky prospect 13, Moscow, 119234 Russia

⁵ Special Astrophysical Observatory, Russian Academy of Sciences, Nizhnii Arkhyz, 369167 Russia

⁶ Department of Physics and Astronomy, N283 ESC, Brigham Young University, Provo, UT 84602, USA

1 November 2021

ABSTRACT

We present observations and models of the kinematics and distribution of neutral hydrogen (HI) in the superthin galaxy FGC 1440 with an optical axial ratio $a/b = 20.4$. Using the Giant Meterwave Radio telescope (GMRT), we imaged the galaxy with a spectral resolution of 1.7 km s^{-1} and a spatial resolution of $15''.9 \times 13''.5$. We find that FGC 1440 has an asymptotic rotational velocity of 141.8 km s^{-1} . The structure of the HI disc in FGC 1440 is that of a typical thin disc warped along the line of sight, but we can not rule out the presence of a central thick HI disc. We find that the dark matter halo in FGC 1440 could be modeled by a pseudo-isothermal (PIS) profile with $R_c/R_d < 2$, where R_c is the core radius of the PIS halo and R_d the exponential stellar disc scale length. We note that in spite of the unusually large axial ratio of FGC 1440, the ratio of the rotational velocity to stellar vertical velocity dispersion, $\frac{V_{\text{Rot}}}{\sigma_z} \sim 5 - 8$, which is comparable to other superthins. Interestingly, unlike previously studied superthin galaxies which are outliers in the $\log_{10}(j_*) - \log_{10}(M_*)$ relation for ordinary bulgeless disc galaxies, FGC 1440 is found to comply with the same. The values of j for the stars, gas and the baryons in FGC 1440 are consistent with those of normal spiral galaxies with similar mass.

Key words: galaxies: individual, galaxies:FGC 1440, galaxies:kinematics and dynamics, galaxies:structure,method:data analysis

1 INTRODUCTION

Superthin galaxies are subset of edge-on low-surface brightness ($\mu_B(0) > 22.7 \text{ mag arcsec}^{-2}$) (Bothun et al. 1997; McGaugh 1996) disc galaxies with an axial ratio $a/b > 10$ (Karachentsev et al. 2003). These late type disc structures observed at high inclination (Matthews et al. 1999; Dalcanton & Bernstein 2000; Dalcanton & Shectman 1996) are some of least evolved disc structure in the Universe (Vorontsov-Vel'yaminov 1974; Kautsch 2009; Uson & Matthews 2003) characterized by ratio of high gas mass to blue luminosity, $\frac{M_{\text{HI}}}{L_B} \approx 1 M_{\odot} L_{\odot}^{-1}$ (Goad & Roberts 1981; Uson & Matthews

2003), and low star formation rates $\sim 0.01 - 0.05 M_{\odot} \text{ yr}^{-1}$ (Narayanan & Banerjee 2021; Wyder et al. 2009).

The HI distribution offers interesting clues to the physical processes regulating the structure, dynamics, and evolution of galaxies. Recent large HI surveys, THINGS (The HI Nearby Galaxy Survey) (Walter et al. 2008), LITTLE THINGS (Local Irregulars That Trace Luminosity Extremes, The HI Nearby Galaxy Survey) (Hunter et al. 2012) have focused on mapping the HI distribution in the nearby spiral and dwarf galaxies, and explain the role of HI in regulating the stability/instability and star formation in these galaxies (Leroy et al. 2008; Bigiel et al. 2008). The high-resolution rotation curves derived in these studies have been used for constraining the dark matter mass in these galaxies (De Blok et al. 2008; Oh et al. 2015). The observed rotation curves in conjunction with the stellar photometry,

* E-mail: kaditya@students.iisertirupati.ac.in

† E-mail: arunima@iisertirupati.ac.in

see for example; SPARC (Spitzer Photometry and Accurate Rotation Curves) (Lelli et al. 2016), and also (Rubin et al. 1980, 1985; De Blok et al. 2001b; Banerjee & Bapat 2017; Kurapati et al. 2018b) have been used to test fundamental scaling relations between the total acceleration and the acceleration due to baryons (Li et al. 2018; Ghari et al. 2019; Li et al. 2019), checking the consistency of Λ -CDM model (Keller & Wadsley 2017) and testing alternate theories of gravity (Gentile et al. 2011; Naik et al. 2019; Chan & Hui 2018). High resolution HI observations may help in better understanding and characterizing instabilities like warps, bars and spiral arms, etc. in gaseous discs of the galaxies (Phookun et al. 1993), also for indirect characterization using Tremaine-Weinberg method, see for example (Banerjee et al. 2013; Patra & Jog 2019). This may also help in uncovering previously unseen gaseous companions, see, for example, detection of satellite galaxy close to NGC 973 in HEROES (HERschel Observations of Edge-on Spirals) survey (Allaert et al. 2015). The observation of HI halos see for example HALOGAS (Hydrogen Accretion in LOcal GALaxieS) survey (Heald et al. 2011) in galaxies provides us with important pointers for understanding the accretion mechanism for replenishing the gas needed for star formation (Voigtländer et al. 2013; Zschaechner et al. 2012; Kamphuis 2008), also see EDGE(Extragalactic Database for Galaxy Evolution survey) - CALIFA (Calar Alto Legacy Integral Field Area) survey (Barrera-Ballesteros et al. 2021; Bolatto et al. 2017).

Measurement of the HI distribution along with the HI dispersion and the radial variation of the scaleheight can be used to model the shape of the dark matter (Olling 1995, 1996). The method was applied to investigate the shape of dark matter halo of eight edge-on gas-rich galaxies with $a/b > 10$ by O'Brien et al. (2010); Peters et al. (2017). Dark matter halo plays an essential role in regulating the structure of the stellar disc; previous studies by Banerjee & Jog (2013); Banerjee et al. (2010) have shown that a compact dark matter halo plays a vital role in regulating the superthin structure and in stabilizing the galactic disc against axis-symmetric instability (Garg & Banerjee 2017; van der Kruit et al. 2001; Ghosh & Jog 2014). Since these galaxies are rich in neutral hydrogen, it contributes significantly to the total potential and plays an important role in regulating the vertical structure of both the stellar and the HI disc (Narayan & Jog 2002). Similarly, the role of HI gas on the stability of galaxy disc was investigated by Jog (1996); Romeo & Falstad (2013). Recent studies have pointed out that the low value of the observed stellar scaleheight is a direct outcome of very low vertical stellar velocity dispersion and that these superthin galaxies are highly stable despite low values of dispersion (Aditya & Banerjee 2021).

Of all the well known superthin galaxies extensively studied in literature till now for the structure of neutral hydrogen, stellar dynamics and properties of dark matter haloes; UGC 7321 (Uson & Matthews 2003; Matthews & Wood 2003; Matthews et al. 1999; Banerjee et al. 2010; Sarkar & Jog 2019a; Aditya & Banerjee 2021; Komanduri et al. 2020; Pohlen et al. 2003) has the highest axial ratio a/b equal to 15.4, followed by FGC 1540 (Kurapati et al. 2018b) which has a/b equal to 12.25. Other superthin galaxies IC 2233 (Matthews & Uson 2008, 2007; Gallagher & Hudson

1976) and IC 5249 (Abe et al. 1999; van der Kruit et al. 2001; Byun 1998; Yock et al. 1999) have an a/b equal to 8.9 and 10.4 respectively.

In this paper, we report HI 21 cm observation of FGC 1440, which has an axial ratio equal to 20.36 (B -band) and is among the flattest known galaxies. To our knowledge, no previous studies have mapped the distribution of the neutral hydrogen studied shape of dark matter halo in such extremely thin galaxies; $a/b \geq 20$. We derive the basic structural and kinematic properties of FGC 1440 by modeling the three-dimensional distribution of the neutral hydrogen in FGC 1440. Comparing different model datacubes, we derive limits on the scaleheight, velocity dispersion, and inclination. We finally use the total rotation curve in conjugation with the stellar photometry to derive constraints on the shape of dark matter density in FGC 1440. Further, using the stellar and the HI surface density, along with the dark matter mass models, we solve the two-component Jeans equation for modeling the vertical stellar dispersion as a function of radius. We use the observed stellar scaleheight and the limits on the HI velocity dispersion and the HI scaleheight as constraints on the two-component Jeans equation (Narayan & Jog 2002; Banerjee et al. 2010; Sarkar & Jog 2020, 2019b; Patra 2020b,a, 2018).

The paper is organized as follows; in §2, we introduce the target FGC 1440, in §3 we discuss the data reduction method, in §4 and §5, we present the analysis of the HI data cube and the results from the modeling of the three-dimensional structure of neutral hydrogen. In §6, we describe the optical photometry of FGC 1440. In §7 and §8, we present the results from mass models and constrain the vertical velocity dispersion using the observed scaleheight in conjugation with the best-fit mass model using the two-component Jeans equation. We finally present the associated discussion in §9 and conclude in §10.

2 TARGET: FGC 1440

FGC 1440 is an edge on disc galaxy included in the ultra flat galaxy catalogue (Karachentseva et al. 2016). Ultra flat galaxies are defined by very large axial ratio $(a/b)_B > 10$, where a/b is the ratio of the major axis to minor axis. The major and minor axes of FGC 1440 (Karachentsev et al. 1993, 2003) in B -band is $a_B \times b_B = 2.24' \times 0.11'$ which gives an $(a/b)_B = 20.36$. FGC 1440 is an edge-on ($i = 90^\circ$) late type Sd spiral galaxy (De Vaucouleurs et al. 1991), located at a distance of 59.6 Mpc (Kourkchi et al. 2020). In a study Hoffman et al. (1989) report an HI diameter 3.8' and further indicate that the ratio of dynamical mass to blue luminosity (M_{dyn}/L_B) is equal to $11.9 M_\odot/L_\odot$, lower limit on the ratio of HI mass to blue luminosity being $M_{HI}/L_B > 0.86 M_\odot/L_\odot$. The HI properties of FGC 1440 have also been delineated in the ALFALFA HI source catalogue, Haynes et al. (2018) report HI flux $F = 9.53 \pm 0.09 \text{ Jy km s}^{-1}$, HI mass $\log(M_{HI}) = 10.08 \pm 0.18 M_\odot$, and $W_{50} = 298 \pm 2 \text{ km s}^{-1}$. In their detailed study on the optical photometry of 47 late-type galaxies Dalcanton & Bernstein (2000, 2002) have observed that FGC 1440 has an extremely small bulge in the center, but they conclude that it might not be a kinematic bulge but rather an edge-on orientation of pseudo-bulge. Further, from their study of vertical color gradients Dal-

Table 1. Basic properties: FGC 1440

Parameter	Value
RA(J2000) ^(a)	12 ^h 28′52.29″
Dec(J2000) ^(b)	+04 ^d 17′35.4″
P.A. ^(c)	53°
a/b ^(d)	20.4
Hubble type ^(e)	Sd
<i>i</i> ^(f)	90°
Distance ^(g)	59.6 Mpc
log (M _{HI} /M _⊙) ^(h)	10.1
W ₅₀ ⁽ⁱ⁾	298 km s ⁻¹
D _{HI} ^(j)	3.8′
M _{HI} /L _B ^(k)	> 0.86
M _{Dyn} /L _B ^(l)	11.8 M _⊙ /L _B

(a,b,c,d): Karachentsev et al. (2003) .

(e): De Vaucouleurs et al. (1991) .

(f): Makarov et al. (2014).

(g): Kourkchi et al. (2020).

(h,i): Haynes et al. (2018).

(j,k,l): Hoffman et al. (1989).

canton et al. (2004) point out that the FGC 1440 might also host concentrated dust lanes. The studies investigating the kinematics of the thick disc in Yoachim & Dalcanton (2008) find that FGC 1440 does not show signatures of a thick disc component, based on their measurement of the off-plane rotation curve, which they find is very similar to the mid-plane rotation curve. We have summarized the basic properties of FGC 1440 in Table 1.

3 OBSERVATIONS AND DATA REDUCTION

We observed FGC 1440 with the Giant Meterwave Radio Telescope (GMRT) on August 19, 2019, for 7 hours (including the overheads) with 26 working antennas. The target FGC 1440 was observed for 5.5 hours in 11 scans of 30 minutes each, interspersed by 11 observations of phase calibrator 1150-003 of five minutes each. The flux calibrator 3C286 was observed at the beginning and the end of the observation for a total of 30 minutes. The observation of the central frequency 1402.5 MHz was done in GSB mode with 512 channels with a spectral resolution of 8.14 kHz (1.71 km s⁻¹) and a total bandwidth of 4.14 MHz. Details of the observation are summarized in Table 2.

3.1 Flagging and Calibration

We perform the data reduction of our GMRT observation using Common Astronomy Software Application (CASA) (McMullin et al. 2007). We begin by flagging the known bad antennae E04, E05, E06, and S02, which were offline during the observation. We then visually inspect the data set and flag the corrupted data. After flagging, we follow the usual procedures for cross-calibration. After cross-calibrating and splitting the ‘target’ from the measurement set, we average the visibilities in time to locate the channels containing the spectral line and then flag those channels to create again a ‘continuum-only’ measurement set which we will use for self-calibration.

Table 2. Summary of FGC 1440 observation

(a) Observing Setup	
Parameter	Value
Observing Date	19 August 2019
Phase center, α (J2000)	12 ^h 28′52.29″
Phase center, δ (J2000)	+04 ^d 17′35.4″
Total on-source observation time	5 $\frac{1}{2}$ hours
Flux calibrator	3C286
Phase calibrator	1150-003
Channel Width	8.14 kHz
Velocity separation	1.7 km s ⁻¹
Central frequency	1400.5 MHz
Total bandwidth	4.14 MHz
(b) Deconvolved Image Characteristics	
Weighing	Briggs
Robustness parameter	0
Synthesized beam FWHM	15.9″ × 13.5″
Synthesized beam position angle	23.1°
rms noise in channel	1.01 mJy/beam

3.2 Imaging the spectral line

We make our zeroth dirty image using CASA task *TCLEAN* and manually mask the emissions. We further do about four rounds of ‘phase-only’ self-calibration and three rounds of ‘amplitude-phase’ self-calibration, lowering the cleaning threshold in each round. We don’t find any improvement in the rms value with further self-calibration and post continuum imaging. We do not detect any continuum emission from the center or around the galaxy FGC 1440. We further apply the final amplitude-phase self-calibration table to the ‘target-only’ measurement set containing both the spectral lines and continuum emissions before performing continuum subtraction using CASA task *UVCONTSUB* with zeroth order interpolation excluding the spectral channels. We create a data cube with the task *tclean* and clean the emission within a mask made by the Source Finding Application (SoFiA, Serra et al. (2015)) down to a level of 0.5 σ . We iterate this process until the SoFiA mask is stable. We have experimented with different weighting schemes in *TCLEAN*, and we find that *briggs* weighing scheme with robustness parameter equal to zero and a *uvtaper* of 10kA gives us the best compromise between resolution and sensitivity. We finally perform Hanning Smoothing on the cube and find that the final resolution of the data cube is 15.9″ × 13.5″, and the rms noise is 1.01 mJy/beam compared to the expected theoretical noise is 1mJy/beam.

4 ANALYSIS

4.1 Global HI profile

In Figure 1, we present the global HI profile of the galaxy FGC 1440. We note that our integrated HI flux 9.6 Jy km s⁻¹ is comparable to that obtained in single dish observation by Haynes et al. (2018). We fit the observed profile using busy-function (Westmeier et al. 2014) to derive the parameters corresponding to the profile. We find that the velocity widths 20% and the 50% of the peak maximum are 304.9

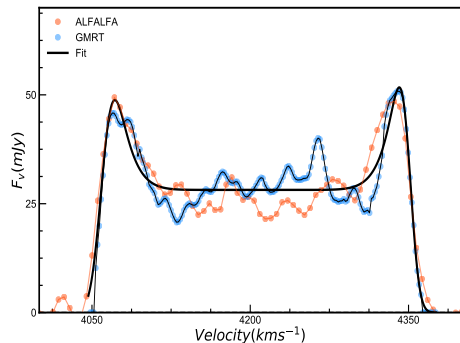


Figure 1. Global HI profile of FGC 1440 derived from our GMRT observation. We have over plotted the fitted busy function on the observed spectrum and indicated the derived profile parameters.

Table 3. Best fit values obtained by fitting busy function.

$V_0^{(a)}$ km s ⁻¹	$W_{50}^{(b)}$ km s ⁻¹	$W_{20}^{(c)}$ km s ⁻¹	$F_{peak}^{(d)}$ mJy	$F_{int}^{(e)}$ Jy km s ⁻¹
4206 ± 1.9	293.3 ± 2.1	304.9 ± 2.94	51.7 ± 3.7	9.6 ± 0.2

- (a): Frequency centroid of the HI line.
- (b): Spectral line width at 50% of the peak flux density.
- (c): Spectral line width at 20% of the peak flux density.
- (d): Peak of the HI flux density.
- (e): Integrated HI flux.

km s⁻¹ and 293.3 km s⁻¹ respectively. The results are summarized in Table 3.

4.2 Channel and moment maps

In Figure 2, we show the channel maps containing the HI emission overlaid on POSS-II (The Palomar Observatory Sky Survey) optical images. In the channels with the highest deviation from the systemic velocity, the emission starts to emanate from the edge of the stellar disc and extends further beyond it. In some channels close to the systemic velocity (70, 102, 106, 110), we see the HI emission extends out of the plane at the center, as compared to the channels further away from the center, for example, the emissions from channels 70, 102 are remarkably extended compared to channels 170, 174, or channels 14 and 18. We will discuss in detail the possible origins of thickening observed in the central channels in §5.4

In Figure 3, we have shown the Moment 0 and the Moment 1 map. We have overlaid the Moment 0 map on the POSS-II optical image. From Moment 0 map, we see a *slight warp on the North-East side of the galaxy*.

5 3D - TILTED RING MODELING

We use the publicly available tilted ring modeling software TiRiFiC (Józsa et al. 2012) for deriving the kinematic and structural properties of FGC 1440. We model the galaxy as a rotating gas disc of radius R with the gas vertical distribution following sech^2 profile. Each ring is set to 1.1 (5.1 kpc) times the beamwidth.

5.1 Modeling strategy

For estimating the initial fit we use Fully Automated TiRiFiC (FAT, Kamphuis et al. 2015) which is GDL wrapper around TiRiFiC. We then further use these initial estimates of the fit parameters and compare the model and data by (1) visually inspecting the emissions in individual channels, (2) comparing the Moment 0 and Moment 1 maps, and (3) the PV diagrams at various offsets to check how well do the model contours match the data. We then further manually vary individual parameters using TiRiFiC while comparing the model and data visually in each iteration. We will now discuss how each kinematics and the structural parameters describing the tilted ring model describing FGC 1440 were chosen.

5.2 Automated Fit using FAT

We have used the beta version of FAT which allows for radial variation of the intrinsic velocity dispersion. FAT takes an HI data cube as an input and automatically estimates the following parameters (free-parameters); 1) surface brightness profile, 2) position angle 3) inclination 4) rotational velocity 4) scaleheight 5) intrinsic dispersion and 5) central coordinates:- right ascension, declination and the systemic velocity. FAT fits each parameter ring by ring and finally smooths the parameters with a polynomial of order 0, 1, 2, 3, 4 or 5. FAT models the HI disc as two halves and fits 9 semi-rings across each half.

The procedure employed by FAT for finding the initial estimates of the free parameters and the flow-chart for fitting is discussed in detail in Kamphuis et al. (2015). FAT fits the surface brightness of the approaching side and the receding side independently and adopts scaleheight equal to $6.1''$. We have summarized the model parameters estimated by FAT in Table 4 and present the plots Figure 4. The rotation velocity (V_{Total}) derived using 3D tilted ring modeling is shown in Figure. 5 overlaid on a major axis PV diagram. After getting an estimate of the kinematic and structural parameters using FAT, we investigate how sensitive the FAT-model is to the variation of each parameter by manually running TiRiFiC, each time changing the fit parameters obtained from FAT and then comparing the model with the data. We find that the model data cube is degenerate for a large range of dispersion values, scale height, and inclination.

5.3 Manual TRM Models

In an attempt to break the degeneracy between the parameters, by constructing a *Flat-Disc* model, We perform several rounds of manual fitting with TiRiFiC followed by visual inspection of channel maps, PV diagrams at various offsets, and the moment maps to estimate the parameters describing the *Flat-Disc* model. The method of iterative visual inspection to routinely carried out to fine-tune the parameter and arrive at the final model data cube see for example Allaert et al. (2015) and also Zschaechner et al. (2012), Gentile et al. (2013), Kamphuis et al. (2013).

Using the model data cube output by FAT as the base model, we iteratively construct model data cubes, each time changing the following parameters; inclination (i), dispersion (σ), and the scaleheight(h_z) in the model output by FAT. In

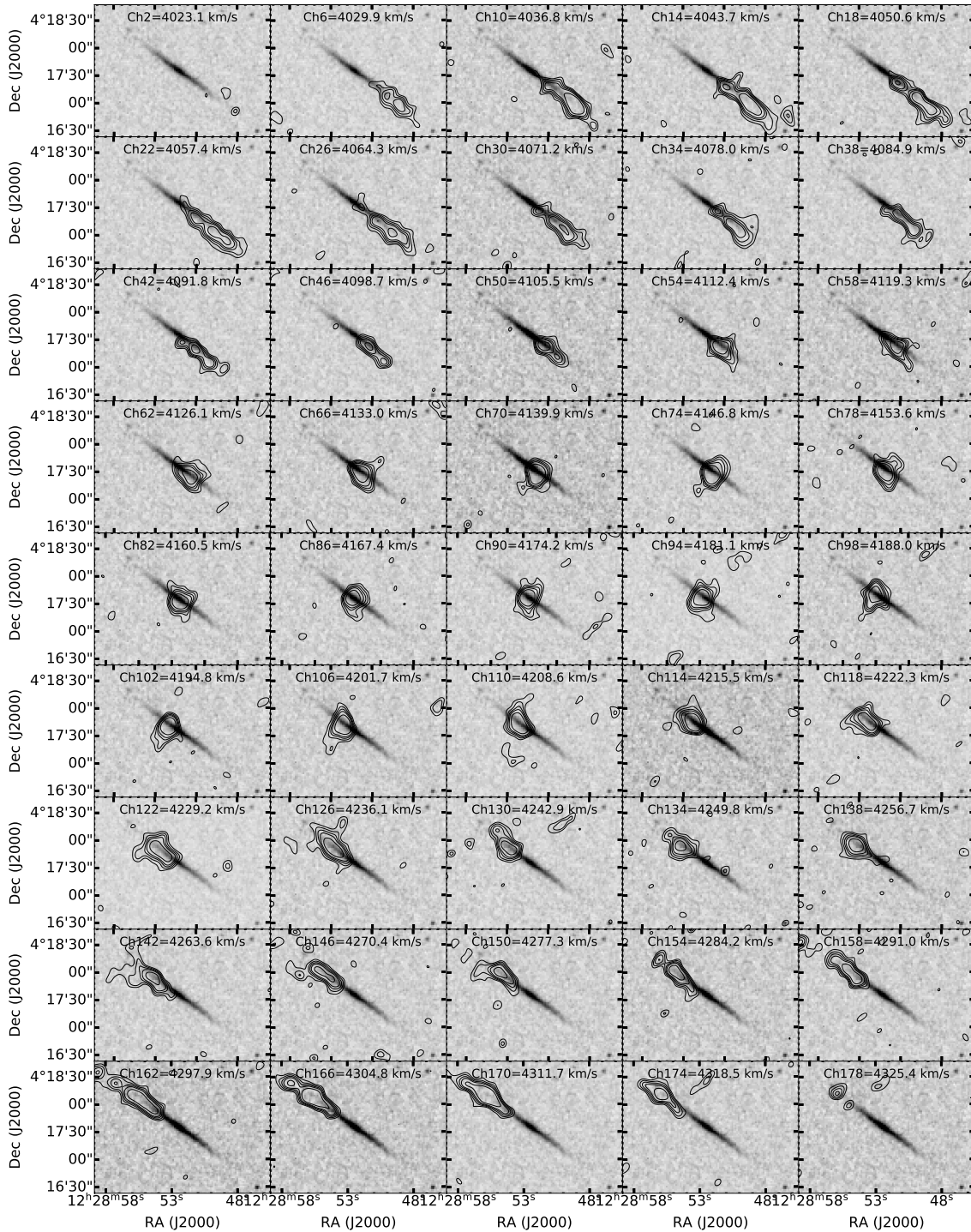


Figure 2. Channel maps showing HI emission from FGC 1440, each panel is separated by four channels. The HI emissions are overlaid on the POSS-II optical image. The contour levels are at $[3, 4, 5, 6] \times 1.01 \text{ mJy beam}^{-1}$

the *Flat-Disc* model, we fix the center's values (RA, Dec), systemic velocity, surface brightness, and position angle to the values derived by FAT. We make different model data cubes by varying the parameters (i, σ, h_z) either one by one, in pairs or all together at the same time. We compare each model with the data through a visual-inspection, wherein we compare the model and data channel-wise, comparing 3D models of data and the model data cubes using volume

rendering software *astroslicer* (Punzo 2017), and comparing the datacube by taking slices at various offsets along the major axis (as it preserves the 3D structure of the cube) to arrive at the secondary base model called the '*Flat-Disc*' model. In Figure 6, we show the Moment 0 and the Moment 1 map derived for the '*flat-disc* model' superposed on the data.

In order to show the effect of varying the inclination (i),

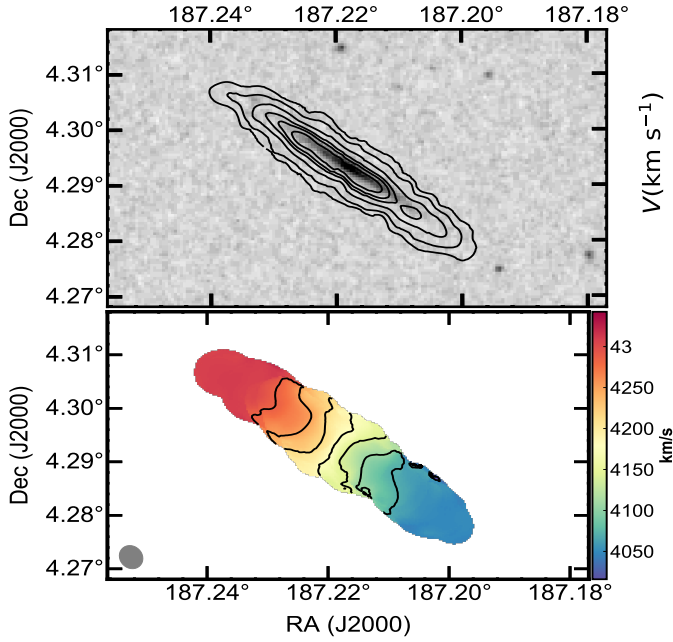


Figure 3. In the top panel we have plotted the Moment0 map the contours are at $[2.5, 5.0, 10, 15, 18, 22] \times 40 \text{ mJy beam}^{-1} \text{ kms}^{-1}$. In the bottom panel, we have shown the Moment 1 map, and the contours start at 4000 kms^{-1} increasing at 35 km s^{-1} .

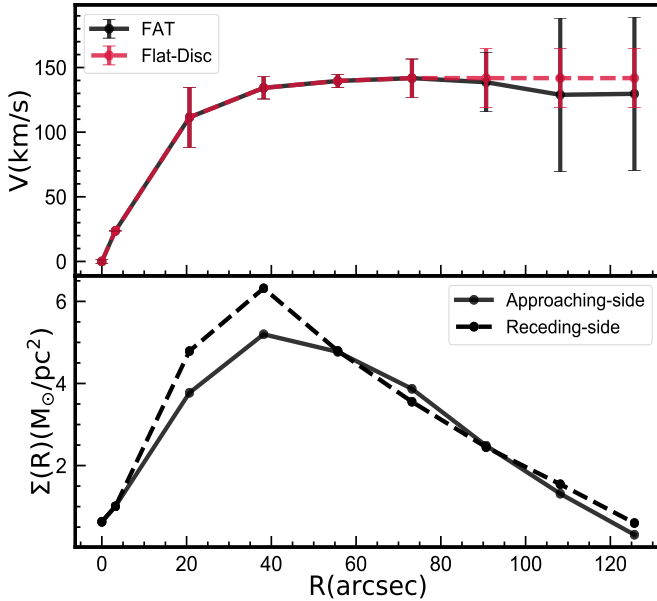


Figure 4. In the above figure we have plotted the rotation velocity and the surface brightness profile obtained from the tilted ring modeling. The surface brightness is fitted independently for the approaching and the receding side.

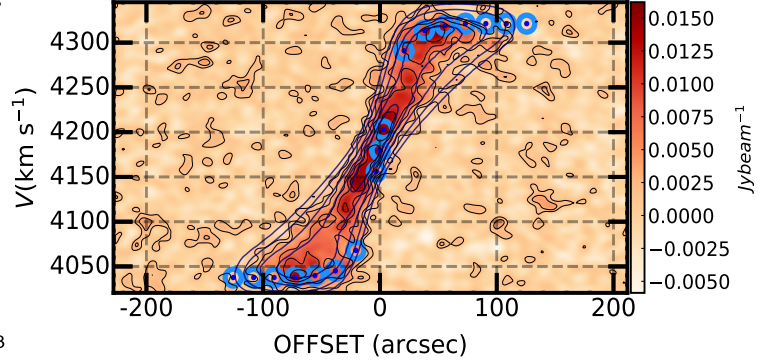


Figure 5. The major axis PV map with flat disc model overlaid at contours $[1.5, 3, 6, 9, 12] \times 1.01 \text{ Jy/beam}$. The blue points describe the HI rotation curve.

Table 4. Parameters describing 'FAT' and 'Flat-Disc' models.

Parameter	FAT-Model	Flat-Disc-Model
X_0^a	+187.2	+187.2
Y_0^b	+4.29	+4.29
i^c	85°	88.5°
V_{sys}^d	4179.45	4179.45
PA^e	53.5°	53.5°
Surface Brightness f	fig 4	fig 4
Dispersion g	6.6 km s^{-1}	15 km s^{-1}
Rotation velocity h	fig 4	fig 4
h_z^i	$6.10'' (1.8 \text{ kpc})$	$0.45'' (0.13 \text{ kpc})$

- a Right ascension
- b Declination
- c Inclination
- d Systemic velocity
- e Position angle
- f Surface brightness as a function of radius
- g Velocity dispersion
- h Rotation velocity as a function of radius
- i Scaleheight of the HI disc

dispersion (σ) and the scaleheight (h_z), we plot the minor axis PV diagrams (Figure 7 to 11) at different offsets, varying each of the parameter (i, σ, h_z), one by one, while keeping the values of the other two-parameters to that of the *Flat-Disc* model (Table. 4). For example, in the second row of the Figure 6, we show the effect of variation of the inclination and how it compares with the data. We keep the values of the dispersion and scaleheight equal to that of the *Flat-Disc* model and vary the values of the inclination. Similarly, in the third row, we keep the values of inclination and scaleheight fixed to that of *Flat-Disc* and vary only the dispersion.

Also, we consider the models in which we vary the values of the inclination, dispersion, and scaleheight as a function of radius, keeping the value of other parameters to be same as that of the '*Flat-Disc*' model;

- **Radially inclination $i(R)$:** The inner rings are kept at an inclination equal to 90° and the outer rings at 85° .

- **Radially varying dispersion $\sigma(R)$:** Dispersion varies from 20 km s^{-1} for the inner rings to 5 km s^{-1} at the outer rings in steps of 5 km s^{-1} .

- **Radially varying scaleheight $h_z(R)$:** The inner rings are kept at an $h_z = 0.45''$, the central rings are kept at $h_z = 1.97''$, and the outer rings at $h_z = 5.3''$.

Inclination (i). For studying the effect of inclination, we fix the values of all the parameters to that of the 'flat disc model' and vary just the inclination to different values. From the minor axis PV diagrams (see Figure 7 to Figure 11), the first immediate observation is that we can rule out the models with an $i < 85^\circ$, for example, the PV plot at an offset equal to 0, Figure 7, the inner model contours at $9 \times \text{rms}$ are not extended sufficiently to describe the emissions and, further models with lower inclination only increase this discrepancy. Comparing the PV diagrams at different offsets, we find that the inclination is restricted in the range $85^\circ < i < 90^\circ$. We note that the inclination value estimated by FAT $i = 85^\circ$ is the lower limit for the inclination of FGC 1440. Models with an inclination lower than 85° do not describe the data accurately.

Dispersion (σ). The value of dispersion is set to 15 km s^{-1} , whereas FAT fits dispersion profile; 6.63 km s^{-1} . By comparing the PV diagrams (figure 7 to 11) we find that the data is not very sensitive to the change in dispersion as the models with dispersion 5 km s^{-1} to 15 km s^{-1} show little variation at the level of data. However, we find that the models with dispersion greater than 15 km s^{-1} clearly start to deviate from the data. We find that the value of the dispersion describing the data is restricted in the range $5 \text{ km s}^{-1} < \sigma_z < 15 \text{ km s}^{-1}$.

Scaleheight (h_z). In Fig. 6 - 9, we observe that the models with higher scaleheight are spatially more extended as compared to models with lower scaleheight, which is more extended along the velocity axis but not spatially. Further, we observe that, in the case of models with higher scaleheight, the model contours do not follow the data contours in the inner regions, i.e., the contours at $9 \times \text{rms}$. The models with lower scaleheight do follow the data contours in the inner regions of the PV diagrams, but it is not easy to distinguish between the models with $h_z = 0.45''$ and $h_z = 1.97''$. We further construct a model with radially varying scaleheight, based on the observation that the inner rings at lower scaleheight give a better description of the data contours in the innermost region of the PV diagram, and the outer rings kept at the higher scaleheight will match the spatially extended data contours in the outer region of the PV diagram. We find the model with radially varying scaleheight is barely distinguishable from models with $h_z = 0.45''$ or $h_z = 1.97''$. To further investigate the vertical structure, in figure 12, we plot the normalized vertical density profile extracted at various slices from the moment 0 maps and overlaid the major axis FWHM of the synthesized beam. We observe that the synthesized beam is comparable to the vertical density profile extracted from the data, thereby indicating that the disc's thickness is barely resolved in these observations. From comparing PV diagrams, we find that the upper limit on scaleheight is $5.3''$.

By comparing the model and data in the minor axis PV diagrams Figure 7 - 11, following above discussion, we find

the lower and upper limits for the values for the inclination ($85^\circ \leq i \leq 88.5^\circ$), dispersion ($5 \text{ km s}^{-1} \leq \sigma \leq 15 \text{ km s}^{-1}$) and the scaleheight ($h_z \leq 5.3''$).

5.4 Thickness of the HI disc

Is it a Flare, thick disc or a line of sight warp ?

In Figure 2, from the channel maps, we observe that the emissions from the channels close to the systemic velocity extend above the plane as compared to the emissions from the end channels, possibly indicating the presence of a thick HI disc or a line of sight warp. We can possibly rule out a flaring disc. The flare would be circular and hence every where along the line of sight. The flare would be better noticeable in the outer channel because the sight line through the outer parts of the disc would be longer and hence the flare is harder to identify in the center. In order to investigate the origin of the observed thickness of the HI disc in the FGC 1440, we make the Moment 0 map considering only the starting channels (4023 km s^{-1} - 4100 km s^{-1}), the central channels close to systemic velocity (4100 - 4242 km s^{-1}) and the end channels (4242 - 4325 km s^{-1}). We then compare the data contours for the said velocity ranges with the model with radially varying scaleheight, inclination, and the flat disc model. We find that the data contours (see Figure 13) are as thin as the model contours in high-velocity channels, indicating that possibly the HI disc in FGC 1440 doesn't show flaring behavior. Further absence of flaring is supported by the observation that instead of the end channels at higher velocities, channels close to the central velocity contribute to the thickness of the HI disc. Thus, a thick HI disc at the center with thickness tapering off radially leaves us only with two options; *that either we are observing a line of sight warp or a thick HI disc at the center.*

In order to further investigate this effect we consider the following models 1) A model with radially varying inclinations and 2) A two-component model with a lagging thick disc ($\frac{dv}{dz} = -10 \text{ km s}^{-1} \text{ kpc}^{-1}$) and ($h_z = 5.3''$) and a thin disc ($h_z = 0.45''$). The value of scaleheight of the thick disc in the two-component model is equal to the upper limit on the scaleheight obtained for the one component model. We then iteratively compare models with data through visual-inspection for different values of $\frac{dv}{dz}$, and find that $\frac{dv}{dz} = -10 \text{ km s}^{-1} \text{ kpc}^{-1}$ better reproduces the data contours. From Figure 13 and 14, we find that overall models with radially varying inclination and the two-component model are very similar; it is barely possible to distinguish if the observed central thickness is the result of radially varying inclination or if the galaxy host central thick HI disc. Further, in Figure.12, we compare the synthesized major axis beam with the density profile, indicating that we possibly can not resolve the thick disc in our observations, although we can not rule out the presence of a central thick HI disc. We adopt a model with a line of sight warp as it is simpler model than the two-component model.

6 OPTICAL PHOTOMETRY

In this section, we present the photometric analysis of FGC 1440 in SDSS g, r band, and UKIDSS K band. As a first step, we mask all the surrounding objects and the galaxy

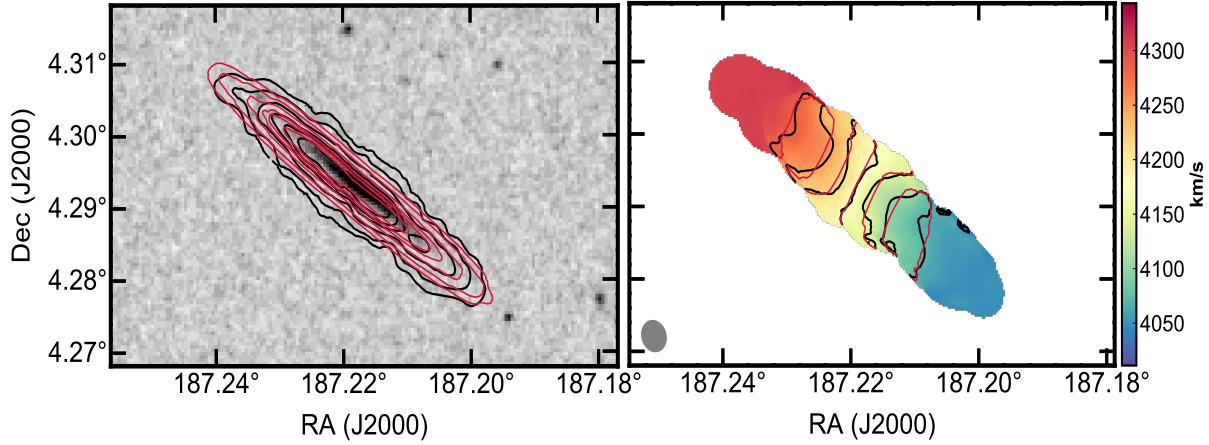


Figure 6. In the top panel we have plotted the moment 0 (top) and the moment 1 (bottom) map the contours are at $[2.5, 5.0, 10, 15, 18, 22] \times 40 \text{ mJy beam}^{-1} \text{ kms}^{-1}$. and the contours for moment 1 map start at 4000 km s^{-1} increasing at 35 km s^{-1} respectively. The contours corresponding to the data are rendered in black and the contours *Flat-Disc-Model* are in shown in red color.

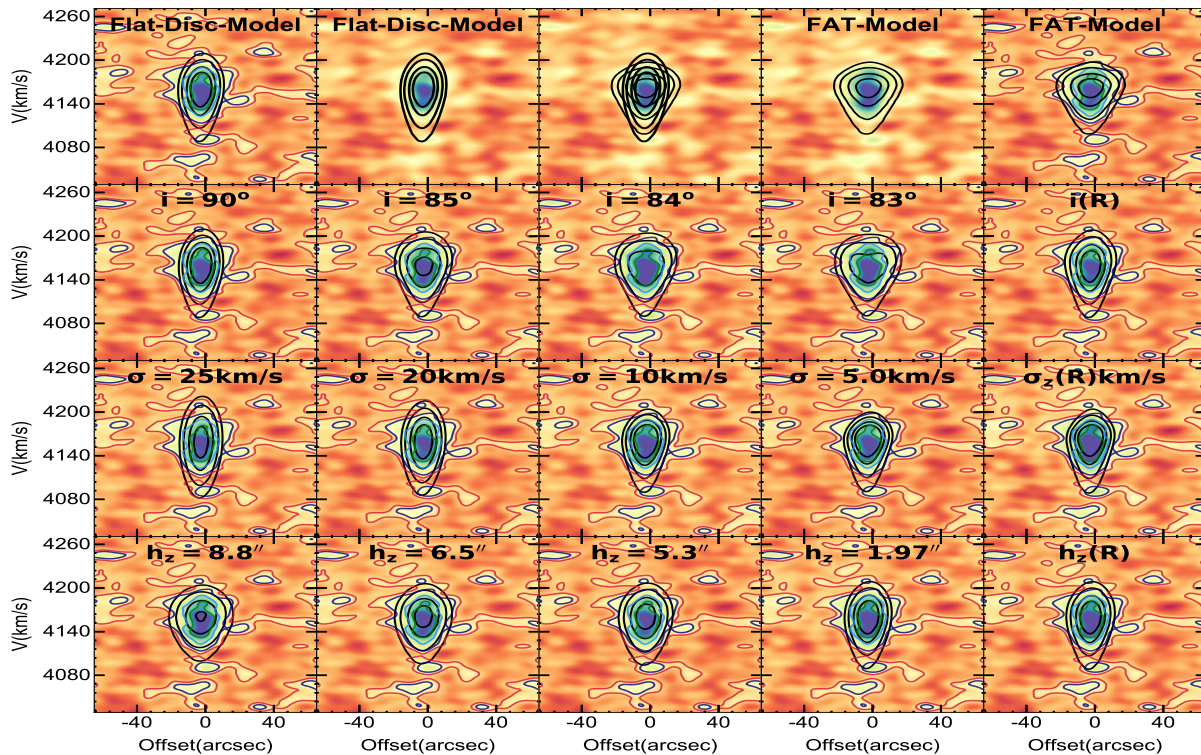


Figure 7. Position velocity maps parallel to the the minor-axis comparing the tilted rings model to data at offset equal to 0 by varying the model parameters. The contours at $[1.5, 3, 6, 9] \times 1.01 \text{ Jy/beam}$.

itself and estimate the positions and the positional angles (PA) using SExtractor (Bertin & Arnouts 1996). We subtract the background by fitting it with a two-dimensional second-order polynomial and then further rotate the entire frame by the PA. Next, we eliminate all the objects lying close to the galaxy by replacing them with the regions symmetric to the galaxy's mid-plane. We then further integrate the light in a rectangular box to estimate the total magnitude. The size of the box was chosen in such a way that the growth curve becomes flat near the borders of the box. The estimated value of the total magnitude in the g, r, and K

bands are 15.43, 14.72, and 11.83. We derive the structural parameters of the galaxy using GalFit (Peng et al. 2011). The intensity profile is $I \sim R/R_d K_1(R/R_d) \text{sech}^2(z/h_z)$, where R_d is the disc scale radius, h_z is the disc scaleheight, and K_1 is the modified Bessel function of the second kind. The parameters derived using optical photometry are summarized in Table 5. The data, the galfit model, and their normalized difference are shown in shown in appendix A.

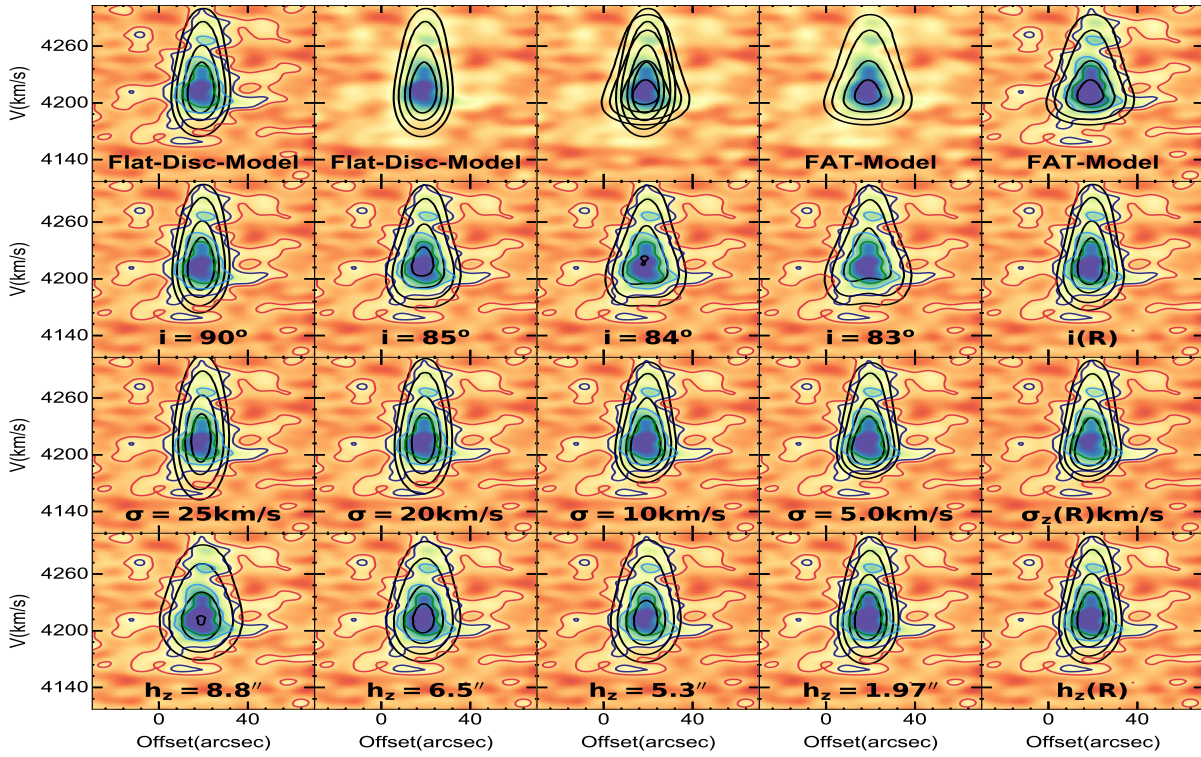


Figure 8. Same as figure 6 but at offset=20

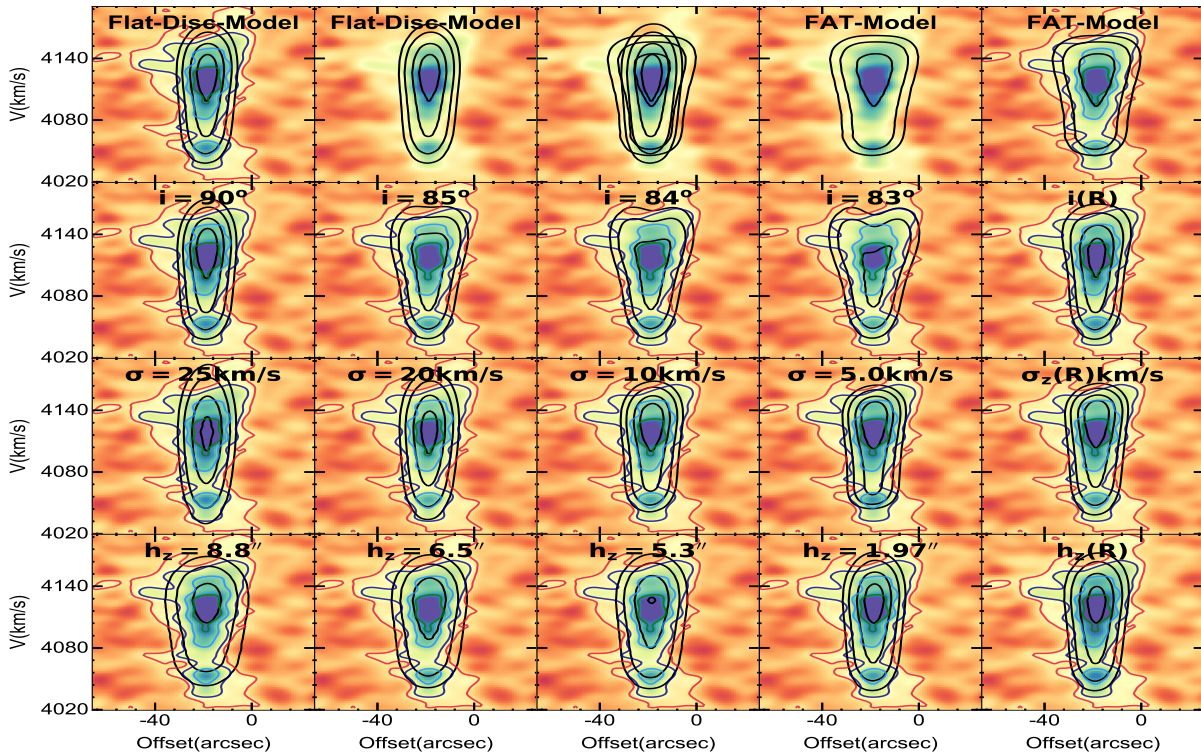


Figure 9. Same as figure 6 but at offset equal to -20.

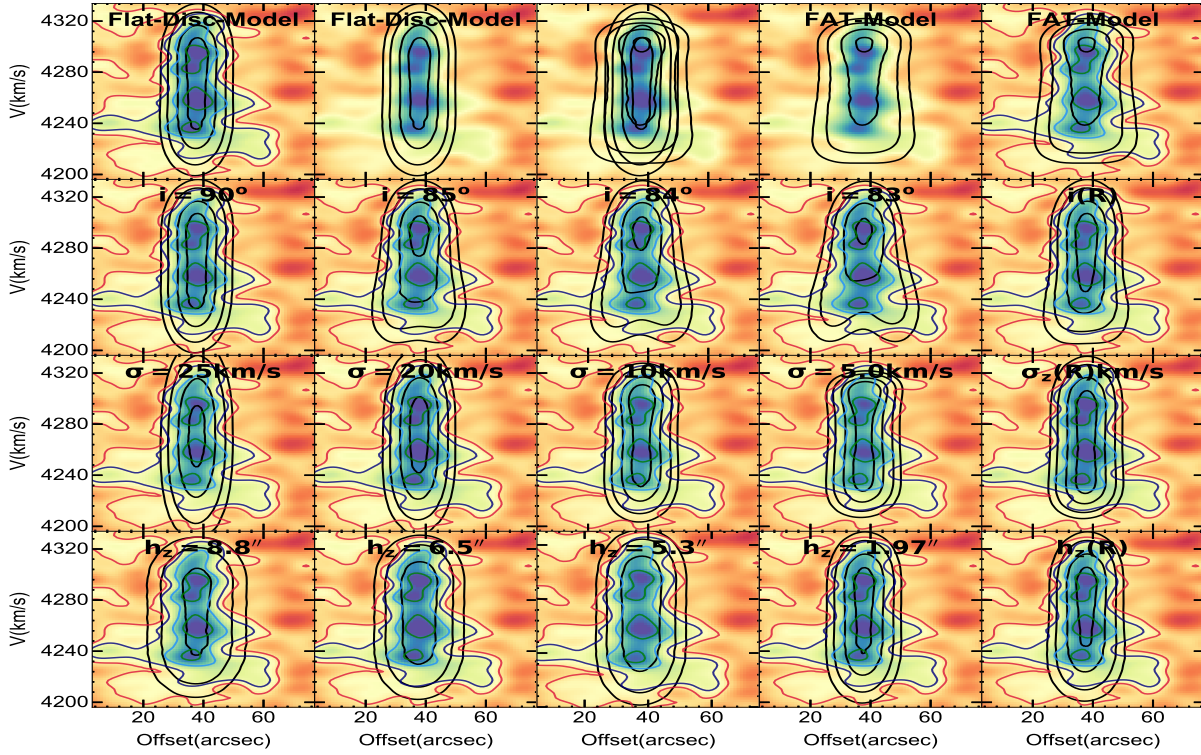


Figure 10. Same as figure 6 but at an offset equal to 40.0

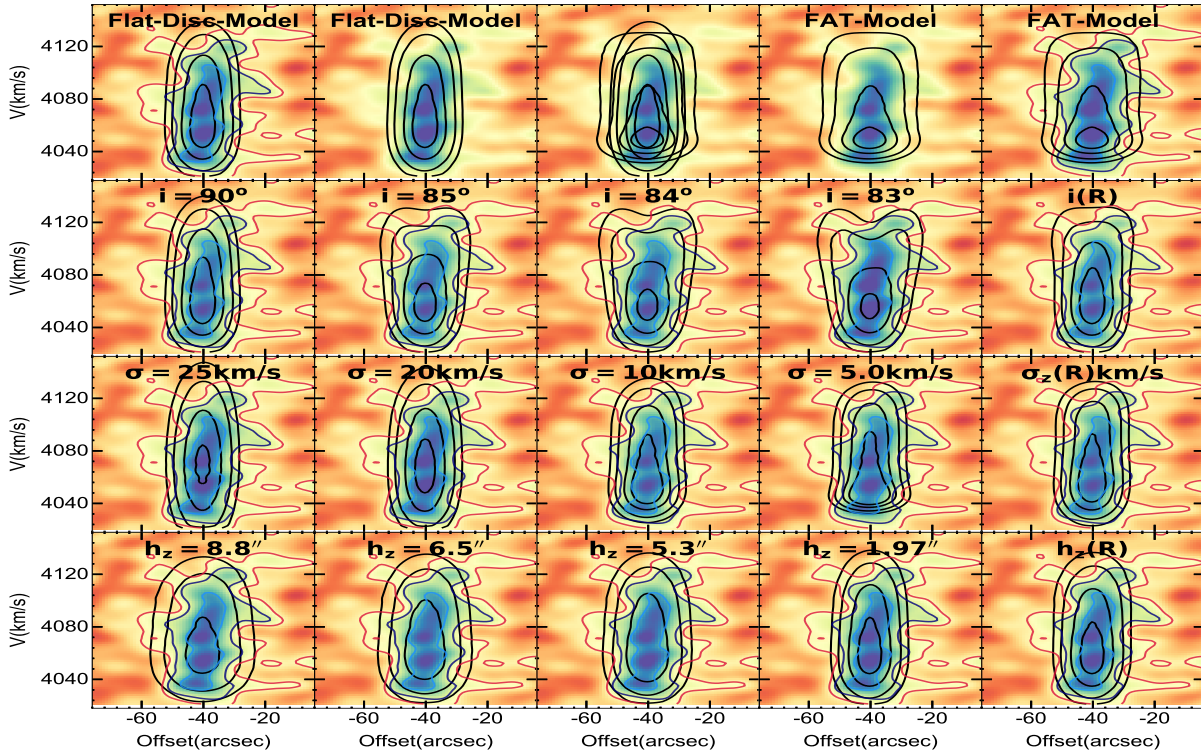


Figure 11. Same as figure 6 but at offset equal to -40.

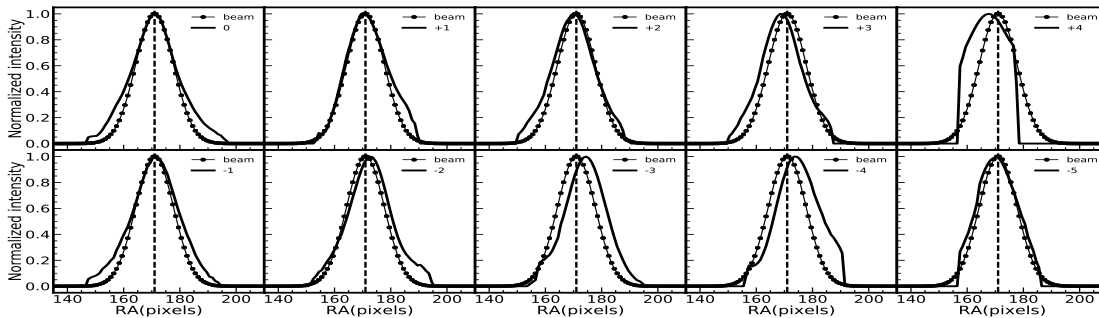


Figure 12. We have compared the synthesized major axis beam size with the vertical density profile at slices extracted from the moment 0 maps.

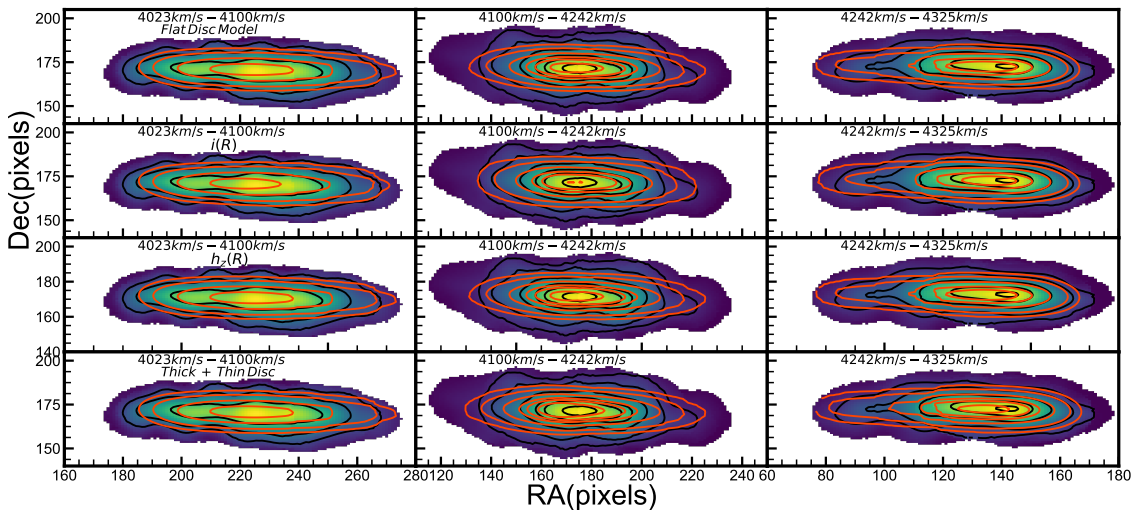


Figure 13. We compare the moment zero maps derived from the central and end velocity channels. In first row we compare the moment maps for the 'Flat-Disc-Model' derived at the velocity range 4023 km s^{-1} to 4100 km s^{-1} the first column and in the middle panel moment 0 map for the central velocity range 4100 km s^{-1} - 4242 km s^{-1} , and in the third panel we show the moment 0 maps for the velocity range 4242 km s^{-1} to 4325 km s^{-1} . Similarly, in the second, third row, and fourth row, we have plotted the contours for the models with radially varying inclination, varying scaleheight, and the two-component model.

7 MASS MODELING

In this section we will present our analysis and results from mass models of FGC 1440. By decomposing the total rotation curve of the galaxy into baryonic (stars+HI) and dark matter components we will determine the contribution of each mass - component to the total rotation curve (V_{Total}) (see Figure 4). The total rotation curve of the galaxy is obtained by adding in quadrature the circular velocity profiles produced by each component separately.

$$V_{Total}^2 = \gamma V_*^2 + V_{gas}^2 + V_{DM}^2 \quad (1)$$

where γ is the mass to light ratio (M/L), V_* , V_{gas} and V_{DM} are the circular velocity profiles due to the stars, gas and dark matter components respectively.

7.1 Neutral gas distribution and rotation curve

We model the gas disc as thin concentric rings and use GIPSY (Van der Hulst et al. 1992) task ROTMOD to derive V_{gas} . We use the surface densities as a function of radius obtained from the tilted ring model (panel 2 Figure 4) as the input parameter in ROTMOD. The gas surface density is scaled by a factor of 1.4 to account for helium and other metals.

7.2 Stellar distribution and rotation curve

For ascertaining the contribution of the stars to the observed rotation curve, we model the stellar distribution in the optical g band and the near-infrared (NIR) UKIDSS K band. We derive mass to light ratio (γ^*) ratio following the empirical relations in Bell et al. (2003) and Bell & de Jong (2001)

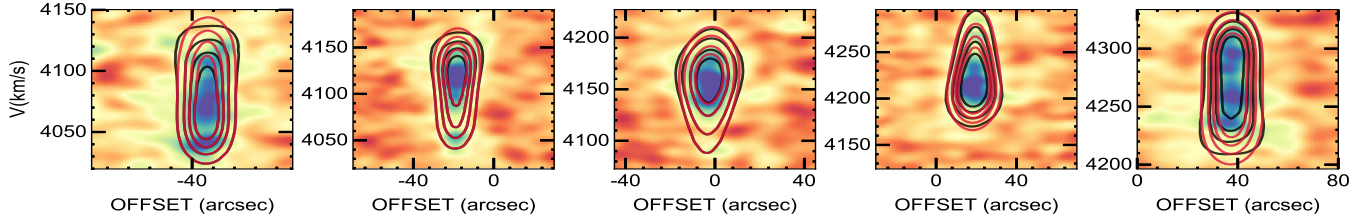


Figure 14. We show the minor axis PV diagrams comparing the model with radially varying inclination and the two-component model. Black contours depict a model with radially varying inclination, and the red contours show the two-component model.

Table 5. Input parameters for deriving the stellar rotation curve.

Parameter	Value g-band	Value r-band	value K-band	Description
Total magnitude	15.4	14.7	11.8	
$\mu_o^{edge-on}$	21.6	20.8	16.5	Edge-on surface brightness in units of $mag/arcsec^2$
$\mu_o^{face-on(*)}$	23.3	22.5	18.6	Face-on surface brightness in units of $mag/arcsec^2$
Σ_o	22.7	31.0	328.0	Surface density in units of L_\odot/pc^2
R_d	4.4	4.2	2.6	Disc scalelength in units of kpc
h_z	0.9	0.9	0.4	Disc scaleheight in units of kpc
Parameters for deriving mass to light ratio (γ^*)				
$g-r$	0.7			
a_λ	-0.5	-0.31	-0.2	Bell et al. (2003)
b_λ	1.5	1.1	0.2	Bell et al. (2003)
γ^*	3.8	3.0	0.8	M/L ratio derived using scaled Salpeter IMF
γ^*	2.7	2.1	0.6	M/L ratio derived using Kroupa IMF

(*): The edge-on surface brightness has been converted to face-on surface brightness using $\mu^{face-on} = \mu^{edge-on} + 2.5 \log(\frac{R_d}{h_z})$ (Kregel et al. 2005).

based on stellar population synthesis models. The scaling between the color magnitude and the mass to light ratio (γ^*)

$$\gamma^* = 10^{(a_\lambda + b_\lambda \times Color)} \quad (2)$$

In the above equation γ^* is the mass to light ratio, a_λ and b_λ are the intercept and slope of the $\log_{10}(\gamma^*)$ versus color calibration obtained by Bell & de Jong (2001) using stellar population synthesis models. We compare the mass models derived using 'dier' Salpeter IMF with the mass models derived using Kroupa IMF (Kroupa 2001). The γ^* ratios assuming Kroupa IMF are derived by subtracting 0.15 dex from the constant term a_λ (table 5). We use the input parameters described in table 5 to derive the stellar rotation curve using the GIPSY task ROTMOD.

7.3 H α Rotation curve

For mass modeling, we derive the hybrid rotation curve, wherein the inner region of the total rotation curve is composed of points from the H α rotation curve, and the HI 21 cm data is used to define the outer points (De Blok et al. 2001a). We have taken the optical rotation for FGC 1440 from Yoachim & Dalcanton (2008). In order to derive a smooth curve passing through the raw optical rotation curve, we fit a simplified multi-parameter function as in Yoachim

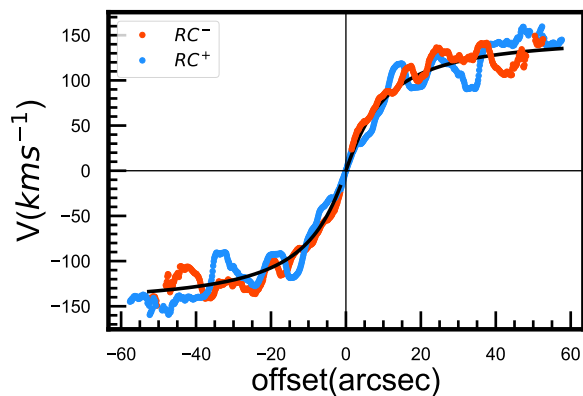


Figure 15. The blue and red points in the above plot depict the optical rotation curve for the approaching and receding side. The points have been mirrored along the major axis. The smooth model optical rotation curve using equation 3 is shown using the solid black line.

& Dalcanton (2005); Courteau (1997),

$$V(r) = V_0 + \frac{V_c}{(1+x^\gamma)^{\frac{1}{\gamma}}} \quad (3)$$

where V_0 is the recession velocity of the galactic center, V_c is the asymptotic rotation velocity (the flat part), x is defines

Table 6. Best fit values describing the Multi-parameter model fitted to raw optical curve.

$V_0^{(a)}$ kms-1	$V_c^{(b)}$ km s ⁻¹	$r_0^{(c)}$ kpc	$r_t^{(d)}$ kpc	$\gamma^{(e)}$
4253.5	149.4±4.2	1.4±0.04	12.3±0.6	1.3±0.1

- (a): Recession velocity at the galaxy center .
 (b): Asymptotic rotation velocity at the flat part .
 (c): Center of the galaxy.
 (d): Point of transition between the rising and the flat part.
 (e): Degree of sharpness of transition.

as $x = r_t/R - r_0$, where r_t is the transition section between the rising and the flat part of the rotation curve and r_0 and γ define the center of the galaxy and degree of sharpness of transition respectively. The best-fitting parameters obtained by fitting Equation 3 to the raw rotation curve are detailed in Table 6. In Figure 15 we show the smooth optical rotation curve and the raw data points.

7.4 Dark matter models

In this work, we parameterize the dark matter distribution using observationally motivated pseudo isothermal (PIS) dark matter halo (Begeman et al. 1991; Fuchs et al. 1998) dominated by a constant density core and, also the Navarro-Frenk-White (NFW) Navarro et al. (1997) dark matter halo profile derived from the cold dark matter (CDM) simulations.

7.4.1 Pseudo-Isothermal halo model

The density profile of the observationally motivated cored spherical pseudo-isothermal (PIS) dark matter halo is,

$$\rho(r) = \frac{\rho_0}{1 + \left(\frac{R}{R_c}\right)^2} \quad (4)$$

where ρ_0 is the central density of the halo and R_c is the core radius. The rotation curve of the PIS halo is given by

$$V(R) = \sqrt{4\pi G \rho_0 R_c^2 \left(1 - \frac{R_c}{R} \arctan\left(\frac{R}{R_c}\right)\right)} \quad (5)$$

where $V_\infty = \sqrt{4\pi G R_c^2 \rho_0}$ is the asymptotic rotation velocity of the dark matter halo. The inner density distribution for PIS halo i.e $R_c \geq R$ is dominated by a constant density core .

7.4.2 NFW halo model

The density distribution of the cuspy NFW dark matter halo derived from the CDM simulations is

$$\frac{\rho(R)}{\rho_{crit}} = \frac{\delta_c}{\left(\frac{R}{R_s}\right)\left(1 + \frac{R}{R_s}\right)^2} \quad (6)$$

where δ_c is the density of the universe at the time of the collapse of the dark matter halo, R_s is the characteristic scale radius, and $\rho_{crit} = 3H^2/8\pi G$ is the critical density of the universe. The inner density of the NFW in the inner radii

$R \leq R_s$ $\rho \neq r^{-1}$, corresponding to steep and cuspy density distribution. The rotation curve due to the NFW density distribution is,

$$V(r) = V_{200} \sqrt{\frac{\ln(1+cx) - cx/(1+cx)}{x[\ln(1+c) - c/(1+c)]}} \quad (7)$$

where, $x = R/R_{200}$, R_{200} is the radius at which the mean density of the dark matter halo is 200 times the critical density. V_{200} is the rotation velocity at R_{200} . The concentration parameter is defined as $c = R_{200}/R_s$.

7.5 Modified Newtonian gravity(MOND)

Apart from the standard dark matter model described in the above section, we use our rotation curve data to test if just the baryonic matter suffices to explain the observed rotation curve in the context of the Modified Newtonian dynamics (MOND) paradigm. The net rotation curve in MOND is given by (Milgrom 1983)

$$V(r) = \sqrt{\frac{1}{\sqrt{2}}(V_{gas}^2 + \gamma^* V_*^2)} \sqrt{1 + \sqrt{1 + \left(\frac{2Ra}{V_{gas}^2 + \gamma^* V_{stars}^2}\right)^2}} \quad (8)$$

where a is acceleration and γ^* is the mass to light ratio.

7.6 Fitting Method

We define the likelihood function as $\exp(-\frac{\chi^2}{2})$, where χ^2 is given by,

$$\chi^2 = \sum_R \frac{\left(V_{obs}(R) - V_T(R)\right)^2}{V_{err}^2} \quad (9)$$

where V_{obs} is the observed rotation curve (see top panel Figure 4), V_T is the total rotation curve (see Equation 1) obtained by adding in quadrature the baryonic and the dark matter components and V_{err} is the error on the observed rotation curve. For optimizing the likelihood function, we use the publicly available python package LMFIT (Newville et al. 2016). The residuals and the corresponding reduced chi-square values χ_{red}^2 are shown in Figures 15 and 16. The HI rotation curve derived for FGC 1440 using 3D tilted ring modeling (section 5.2) has few points in the inner region of the galaxy, and the slope of the dark matter density critically depends on the shape of the rotation curve in the inner region i.e. a steeply rising or slowly rising rotation curve. In order to overcome this problem we use the $H\alpha$ rotation curve in the inner region and the points from the HI rotation curve in the outer region, where the $H\alpha$ data is not available. Although the shape of the $H\alpha$ rotation curve is well defined, in order to account for the scatter between the points, we derive a smooth representation of the $H\alpha$ rotation curve (§7.3). Further, to derive the hybrid rotation curve consisting of the points from the smooth $H\alpha$ rotation curve in the inner region and the HI rotation curve in the outer region, we use B-spline method from python package scipy (Virtanen et al. 2020) and create a smooth spline approximation of the data. Further, in order to gauge the effectiveness of using the hybrid rotation curve for estimating the dark matter parameters and mass models, we also derive

the mass models constrained by the HI rotation curve only, the results of which are shown in Appendix-B. We find that the results using only the HI rotation curve and those using the hybrid rotation curve are comparable. We assume uniform error bars equal to 10 km s^{-1} for the data points defining the observed rotation curve as these are typical conservative error estimates, see for example (De Naray et al. 2008; Mc-Gaugh et al. 2001), also McGaugh et al. (2001) show that the halo parameters are robust against precise definition of the error-bars.

In case when the dark matter distribution is parameterized using the pseudo-isothermal dark matter halo, the free parameters are ρ_0 and R_c , and mass to light ratio γ^* along with ρ_0 and R_c in case of mass, models derived keeping the mass to light ratio as a free parameter. When the dark matter density is parameterized using the NFW halo, the free parameters are c and R_{200} , and γ^* is the free parameter along with c and R_{200} in case of mass models in which the mass to light ratio is kept as a free parameter.

7.7 Results from mass modeling

This section presents the mass models constructed using the SDSS optical g-band and NIR K-band rotation curve in conjunction with the derived HI and the total rotation curve as detailed in the above sections. For each of the photometric band, we fit both the NFW and PIS dark matter halo profile and discuss the following cases:

- **The constant γ^*** We derive γ^* using population synthesis models as described by Bell & de Jong (2001).
 - a) diet – Salpeter IMF which gives highest disc mass for a given photometric band (De Blok et al. 2008) and
 - b) Kroupa IMF which produces lower disc mass Kroupa (2001) as compared to 'diet – Salpeter IMF'.
- **Free γ^*** In this model, the γ^* is kept as a free parameter along with the parameters corresponding to the dark matter density profile.
- **Maximum Disc** We scale the stellar rotation curve by scaling the γ^* such that the observed rotation curve in the inner region is entirely due to the stellar component. The maximum disc model sets the lower limits on the dark matter density.
- **Minimum Disc** We set the contribution of the gaseous disc and stars to zero and attribute the observed rotation curve to be entirely due to the underlying dark matter distribution. The minimum disc model sets the upper limit on the dark matter density.

In Figure 16, we present mass models constructed using the stellar rotation curve derived using g-band Photometry and the HI rotation curve. We find that the reduced chi square (χ_{red}^2) for the cored pseudo-isothermal dark matter halo is lower than the cuspy NFW dark matter halo, only in the case of the model derived using 'diet – Salpeter IMF' both the halos give similar (χ_{red}^2) values. For mass models using PIS halo, we find that the Kroupa IMF gives lower reduced (χ_{red}^2) as compared to the 'diet – Salpeter IMF', indicating that the mass distribution is possibly dominated by dark matter. In mass models for PIS halo with γ^* as a free parameter, γ^* values tend to values closer to that derived using the 'diet – Salpeter IMF'. In case of the mass models with NFW halo and γ^* kept as a free

parameter, we find that the γ^* tends to values higher than that derived using the stellar population synthesis models. In the case of the maximum disc models, we have scaled the stellar rotation curve by a factor of 14 to maximize the contribution of the stellar disc and set the baryonic to zero in the case of the minimum disc models.

Similarly, in Figure 17, we present the results from mass models using the stellar rotation curve in K-band. The χ_{red}^2 for the mass model with PIS dark matter halo is systematically lower than that corresponding to the NFW dark matter halo. The χ_{red}^2 for the Kroupa IMF is lower than that for 'diet – Salpeter IMF'. Whereas in the case of mass models with γ^* as a free parameter, γ^* is even lower than that derived using Kroupa IMF in the case of both PIS halo and NFW halo, possibly indicating the mass models prefer lighter IMF in K-band. We scale the stellar rotation curve by a factor of 1.1 to derive the maximum disc model and set the baryonic contribution to zero for the minimum disc models.

The definition of compact dark matter halo follows from the ratio of the core radius to the disc scalelength $R_c/R_d < 2$ (Banerjee & Bapat 2017). In table 7, we have indicated R_c/R_d for each model, in all the cases other than the maximum disc case in K-band R_c/R_d is less than 2. We also note that the definition of a compact halo is not independent of the choice of IMF, as models which prefer maximum disc in a given photometric band have a larger core radius and less compact dark matter halo.

For models with constant IMF, we find that the concentration parameter ranges between 2.8 (diet-Salpeter K-band) and 5.5 (Kroupa IMF in g-band). Similar to the compactness parameter, the IMF models preferring higher disc masses have smaller concentration parameters. The scaling between asymptotic rotation velocity V_{max} and concentration parameter given in Bottema & Peñano (2015) $c_{exp} = 55.5(V_{max}/[kms^{-1}])^{-0.2933}$, gives us $c = 12.97$. We note that the value of concentration parameters derived in this work are much lower than the value predicted by the scaling. Similarly the using the scaling between V_{max} and R_{200} , where $R_{200} = 0.0127(V_{max})^{1.37}c_{exp}$ gives $R_{200} = 146kpc$ which is closer to the values of R_{200} obtained in case of maximum disc models. We also derive mass models using HI rotation curve derived using the tilted ring models, see Appendix- B, we find that the reduced $\chi_{reduced}^2$ for the PIS halo is smaller than that obtained for the NFW halo.

We further compare our results with theoretical predictions between the ratio of V_{max}/V_{200} and concentration parameter from Dutton & Maccio (2014). The relation between V_{max}/V_{200} and concentration parameter c is defined as $V_{max}/V_{200} = 0.216c_{200}/f(c_{200})$, where $f(c_{200}) = \ln(1+c) - c/(1+c)$. Using the the values of concentration parameter from Table. 7, we find that the value of V_{max}/V_{200} is close to 1.

We test for the correlation between the dark matter core radius and the disc scalelength using the relation given in Donato et al. (2004) $\log(R_c) = (1.05 \pm 0.11)\log(R_d) + (0.33 \pm 0.04)$. With K-band disc scalelength $R_d = 2.58kpc$ we get a core radius equal to 5.78 kpc, which is closer to the diet-Salpeter and the maximum disc case. Similarly the g-band scalelength gives core radius equal to 10.72 kpc.

Table 7. Dark matter density parameters derived from mass-modeling using the optical g-band and NIR K band photometry using the hybrid (HI + H α) rotation curve.

Model	$c^{(a)}$	$R_{200}^{(b)}$ (kpc)	$\gamma^{*(c)}$	$\frac{V_{max}}{V_{200}}^{(d)}$	$\chi_{red}^{2(e)}$	$\rho_0^{(f)} \times 10^{-3}$ M_{\odot}/pc^3	$R_c^{(g)}$ (kpc)	$\gamma^{*(h)}$	$\frac{R_c}{R_d}^{(i)}$	$\chi_{red}^{2(j)}$
g-band	NFW profile					PIS profile				
'diet' Salpeter	5.06 ± 0.5	84.1 ± 0.3	3.8	2.3	0.1	56.6 ± 0.4	2.3 ± 0.01	3.8	0.5	0.1
Kroupa IMF	5.5 ± 0.06	84.4 ± 0.3	2.7	2.3	0.1	66.1 ± 0.6	2.2 ± 0.01	2.7	0.5	0.01
Free γ^*	3.8 ± 0.1	85.0 ± 0.3	6.4 ± 0.2	2.3	0.05	58.0 ± 0.61	2.3 ± 0.01	3.6 ± 0.05	0.5	0.01
Maximum Disc	0.06 ± 0.04	218.4 ± 9.6	14	0.07	0.3	1.4 ± 0.05	19.2 ± 0.8	14	4.3	0.2
Minimum Disc	5.7 ± 0.06	96.1 ± 0.3	0	2.0	0.1	71.9 ± 0.43	2.4 ± 0.0	0	0.5	0.9
K-Band										
'diet' Salpeter	2.8 ± 0.09	97.0 ± 1.3	0.5	2.01	0.4	13.9 ± 0.4	4.9 ± 0.09	0.85	1.9	0.14
Kroupa IMF	3.8 ± 0.09	91.6 ± 0.8	0.6	2.1	0.3	24.3 ± 0.5	3.7 ± 0.05	0.6	1.	0.08
Free γ^*	5.6 ± 0.2	87.9 ± 0.6	0.2 ± 0.04	2.2	0.2	38.8 ± 2.7	3.02 ± 0.11	0.4 ± 0.03	1.2	0.1
Maximum Disc	1.6 ± 0.10	128.9 ± 3.6	1.1	1.5	0.6	8.5 ± 0.3	6.7 ± 0.2	1.1	2.6	0.3
Minimum Disc	5.7 ± 0.06	96.1 ± 0.3	0	2.0	0.1	71.8 ± 0.4	2.4 ± 0.0	0	0.9	0.1
MOND										
	$a^{(k)}$ ms^{-2}	$\gamma^{*(l)}$	$\chi_{red}^{2(m)}$							
g-Band	0.42×10^{-10}	12.7 ± 0.1	0.2							
g - Band ^{a=fixed}	1.2×10^{-10}	4.1 ± 0.1	1.8							
K-Band	0.85×10^{-10}	1.0	0.5							
K - Band ^{a=fixed}	1.2×10^{-10}	0.6 ± 0.01	0.8							

(a): Concentration parameter of the NFW profile

(b): Radius at which the mean density equal to 200 times the critical density.

(c): Mass to light ratio derived using population synthesis models or estimated as a free parameter.

(d): Ratio of the asymptotic velocity to the velocity at $\frac{V_{200}}{km\ s^{-1}} = 0.73 \frac{R_{200}}{kpc}$ (Navarro et al. 1997)

(e): Reduced chi-square value corresponding to the fit.

(f): The central dark matter density of the PIS dark matter halo model

(g): The core radius of the PIS dark matter halo model

(h): Mass to light ratio derived using population synthesis models or estimated as a free parameter.

(i): Ratio of the core radius and the disc scalelength.

(j): Reduced chi square value corresponding to the fit.

(k): Acceleration per lenght in MOND.

(l): Estimated Mass to light ratio in MOND.

(m): Reduced chi square corresponding to the fit.

We compare the parameters $V_{\infty} = \sqrt{4\pi G \rho_0 R_c^2}$ for the PIS halo and $R_s = R_{200}/c$ of FGC 1440 with the that of other superthins in the literature as R_s and V_{∞} constitute single parameter encompassing both the fit parameters. In the study of three superthins Banerjee & Bapat (2017) find V_{∞} equal to 110 km s⁻¹, 112 km s⁻¹ and 99 km s⁻¹ for UGC7321, IC5249 and IC2233 respectively. In another another study, Kurapati et al. (2018b) find V_{∞} equal to 82.7 km s⁻¹ for FGC 1540. We find $V_{\infty} = 135$ for FGC 1440. Banerjee & Bapat (2017) find R_s equal to 8.55 and 22.6 for UGC 7321 and IC 5249, Kurapati et al. (2018b) find R_s equal to 5.25 for FGC 1540. For FGC 1440, we find R_s equal to 24.3.

7.7.1 Mass models MOND

In the last panels of figures 16 and 17, we have shown the mass models derived using MOND. Keeping both a and γ^* as a free parameter we find that the, acceleration parameter $a = 0.42 \times 10^{-10} ms^{-2}$ and $\gamma^* = 12.7$ in g-band. Similarly in K-band the acceleration parameter $a = 0.85 \times 10^{-10} ms^{-2}$ and

$\gamma^* = 0.97$. We note that in the case when both the a and γ^* are kept as free parameters, γ^* tends to values maximizing the disc mass, i.e., they are closer to the maximum disc case of dark matter models. We also try the case in which we fix the value of $a = 1.2 \times 10^{-10} ms^{-2}$ and only vary γ^* , we find that the value of γ^* is equal to 4.14 and 0.65 in g-band and K-band respectively, and is closer to the values derived using population synthesis models.

8 VERTICAL STRUCTURE OF FGC 1440.

We model the galaxy disc as a co-planar, co-axial gravitationally coupled *star + gas* system under the influence of the force field of external dark matter halo. Solving the two-component Jeans equation using the methods outlined in Aditya & Banerjee (2021) and Komanduri et al. (2020) we derive the stellar vertical velocity dispersion (σ_z) as function of radius constrained by the observed stellar scaleheight. We use the best fitting mass model, i.e., the pseudo-isothermal (PIS) profile with stellar surface density scaled by Kroupa

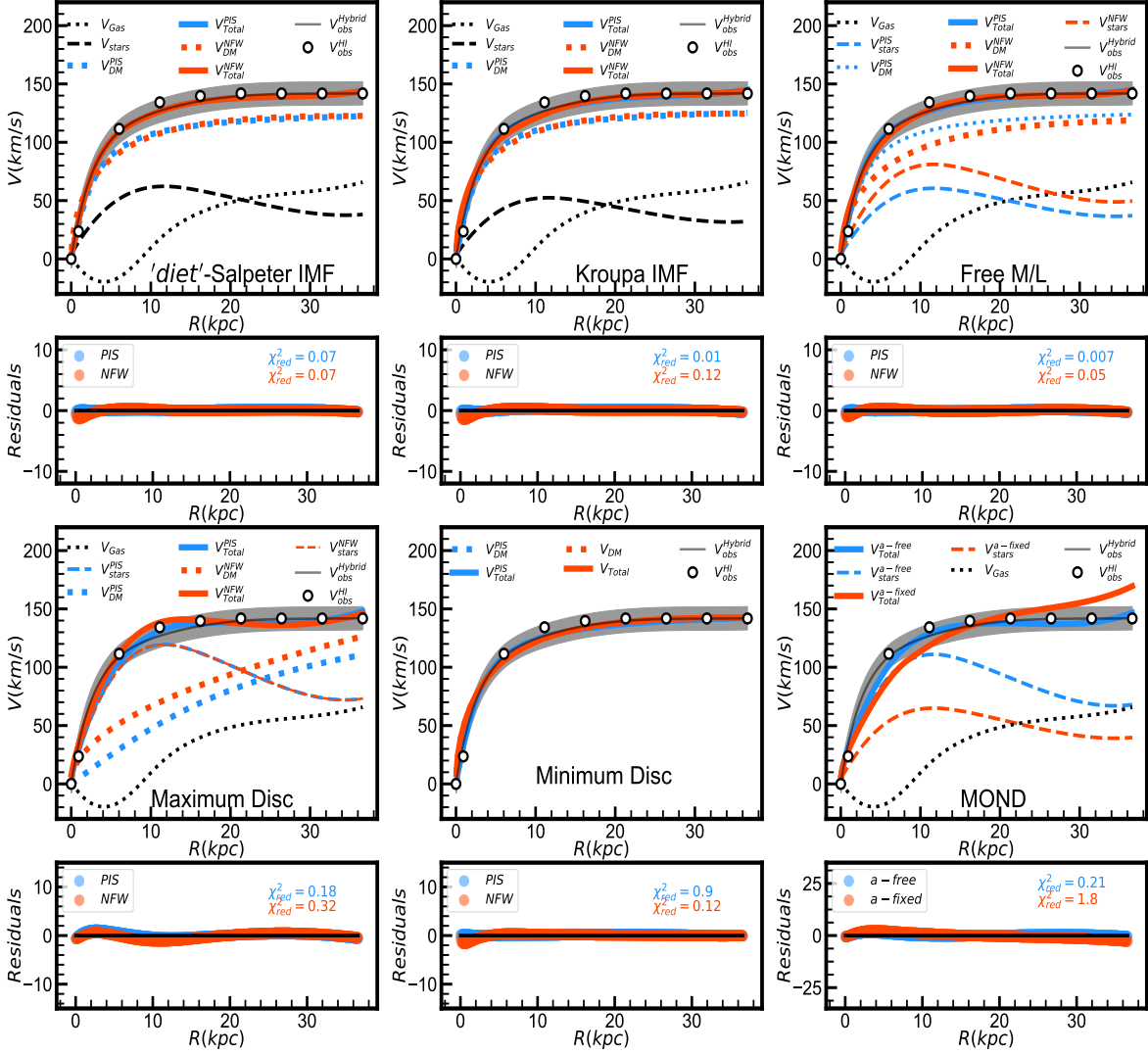


Figure 16. We present the mass model of the galaxy FGC 1440 derived using SDSS g-band photometry. The mass models are constrained using the hybrid rotation curve.

IMF, along with the observed HI surface density and the HI dispersion as the input parameters. From the 3-D models of the HI data cube, we find that the HI dispersion is constrained in the range $5\text{km s}^{-1} < \sigma_{HI} < 15\text{km s}^{-1}$, so we model the stellar vertical dispersion fixing the HI dispersion at 5km s^{-1} , 10km s^{-1} , 15km s^{-1} at all radius. The stellar dispersion is modeled as an exponential function $\sigma_z(R) = \sigma_0 e^{-\frac{R}{\alpha R_d}}$, where σ_0 is the central dispersion and the α is the steepness parameter. The values of the σ_0 and α derived using the mass models in g-band, and K-band are summarized in Table

8. We find that the central value of the stellar dispersion is not sensitive to the variation of the σ_{HI} in the allowed range, but the steepness parameter is. The steepness parameter (α) varies between for $3.2 - 4.2$ in g-band and $4.2 - 6.3$ in K-band for $5\text{km s}^{-1} < \sigma_{HI} < 15\text{km s}^{-1}$. For the different values of the σ_{HI} , we find that the modeled stellar scaleheight agrees with the observed scaleheight up to $3R_d$. For the values of $\sigma_{HI} = 5\text{km s}^{-1}$ we find that the model predicted HI scaleheight (panel 3 in Figure 17) is constrained between the limits obtained from tilted ring modeling ($0.45'' < h_z < 5.3''$).

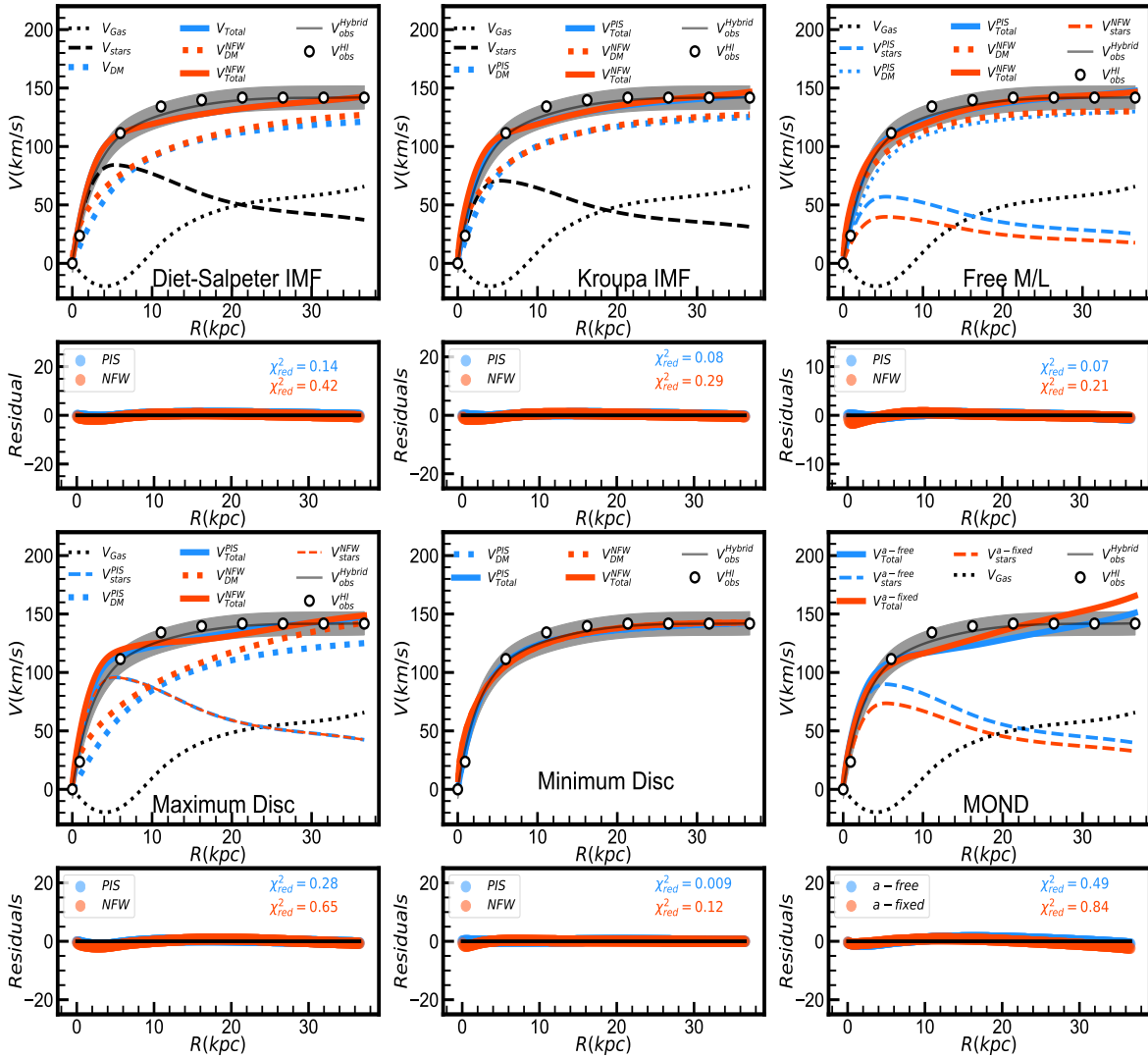


Figure 17. We present the mass-model of the galaxy FGC 1440 derived using UKIDSS K-band photometry. The mass models are constrained using the hybrid rotation curve.

Table 8. Values of vertical stellar dispersion.

Parameter	g-Band		K-Band	
	σ_0 km s ⁻¹	α	σ_0 km s ⁻¹	α
$\sigma_{HI}=5$ km s ⁻¹	29.0	4.2	18.6	6.3
$\sigma_{HI}=10$ km s ⁻¹	29.7	3.6	19.1	4.8
$\sigma_{HI}=15$ km s ⁻¹	29.9	3.2	20.1	4.2

9 DISCUSSION

• In this Section we discuss the main dynamical properties of FGC 1440, and compare them with those determined in the literature for other superthin galaxies.

– Disc Heating

It has been shown that bars, spiral arms, and globular clusters play an important role in disc heating. Bars and spiral arms heat the disc in the radial direction whereas globular clusters heat the disc isotropically in both the radial and vertical direction (Aumer et al. 2016; Jenkins

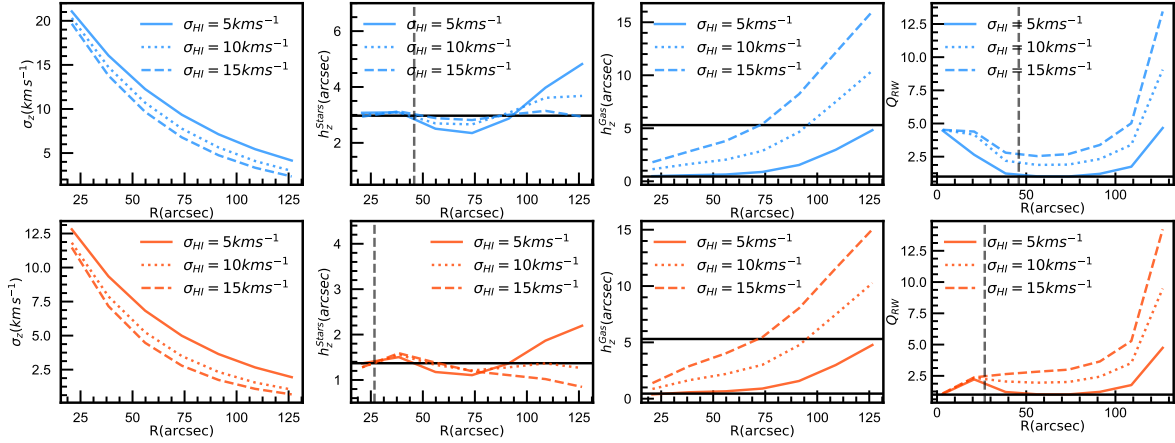


Figure 18. The plots show the vertical velocity dispersion σ_z , the modeled stellar (h_z^{stars}) and HI scaleheights (h_z^{Gas}), and the stability parameter (Q). The top panel in blue ink depicts the results for g-band and lower panel in red, the results in K-band. The vertical dashed line marks the $3R_d$ in g-band and K-band respectively. The horizontal black line in panel depicting h_z^{stars} marks the observed stellar scaleheight. The horizontal line in plot showing h_z^{Gas} marks the upper and the lower limit on the HI scaleheight derived using the tilted ring modeling.

& Binney 1990; Grand et al. 2016; Saha 2014). Further, Banerjee & Jog (2013) showed that a compact dark matter halo regulates the distribution of the stars in the vertical direction and gives rise to superthin disc structure. Aditya & Banerjee (2021) show for a sample of superthin galaxies that the absolute values of the vertical stellar velocity dispersion is small as compared to the Milky way. And upon comparing the the ratio of vertical velocity dispersion to the total rotation velocity ($\frac{V_{Rot}}{\sigma_z}$), they find that the value of $\frac{V_{Rot}}{\sigma_z}$ is comparable to stars in the thin disc of Milky way, indicating that superthin galaxies are dynamically cold systems. Thus, it is imperative to compare the value of $\frac{V_{Rot}}{\sigma_z}$ for FGC 1440 with previously studied superthin galaxies to quantify the effect of the disc heating. Using the values of vertical velocity dispersion constrained using optical photometry; we find that the ratio $\frac{V_{Rot}}{\sigma_z}$ for FGC 1440 is comparable to the sample of superthin galaxies studied in Aditya & Banerjee (2021) equal to 5.0, except for UGC 7321 which has $\frac{V_{Rot}}{\sigma_z} = 10$. Similarly using the values of the velocity dispersion constrained with the g-band and K-band data we find that value of $\frac{V_{Rot}}{\sigma_z} = 8$ for FGC 1440 compared to 10 for other superthin galaxies, except for IC2233 which has $\frac{V_{Rot}}{\sigma_z} = 14$ and UGC00711 which has $\frac{V_{Rot}}{\sigma_z} = 5$.

– Disc dynamical stability

The disc dynamical stability Q as quantified by Toomre (1964) $Q = \frac{\kappa\sigma}{\pi G\Sigma}$, where Toomre stability criterion ‘ Q ’ is a subtle balance between the epicyclic frequency of the self-gravitating matter κ , the radial velocity dispersion σ and the surface density Σ . The epicyclic frequency κ at a radius R is defined as $\kappa^2(R) = (R\frac{d\Omega(R)}{dR} + 4\Omega(R)^2)$, where Ω is the angular frequency defined as $\Omega(R)^2 = \frac{1}{R}\frac{d\Phi_{Total}}{dR} = \frac{V_{Rot}^2}{R^2}$. Φ_{Total} is the total gravitational potential and V_{Rot} is the total rotation velocity.

Garg & Banerjee (2017) show that dark matter plays

a decisive role in regulating the stability of the low surface brightness galaxies and that in the absence of dark matter, the galaxy disc would be susceptible to axis-symmetric instabilities. Further, in Aditya & Banerjee (2021) it has been shown for a sample of superthin galaxies that the median values of stability for the *star + gas* system is higher than the typical spiral galaxies studied by Romeo & Mogotsi (2017). This section compares the value of the stability of the *star + gas* disc of FGC 1440 with that of previously studied superthin galaxies. Using the two-component stability parameter derived in Romeo & Wiegert (2011), we compute the dynamical stability of the *star + gas* system for FGC 1440.

The two-component disc stability parameter Q_{RW} appraising the stability of the composite *star + gas* disc is given by

$$\frac{1}{Q_{RW}} = \begin{cases} \frac{W_\sigma}{T_s Q_s} + \frac{1}{T_g Q_g} & \text{if } T_s Q_s > T_g Q_g \\ \frac{1}{T_s Q_s} + \frac{W_\sigma}{T_g Q_g} & \text{if } T_s Q_s < T_g Q_g \end{cases} \quad (10)$$

where the weight function W is given by

$$W_\sigma = \frac{2\sigma_s\sigma_g}{\sigma_s^2 + \sigma_g^2} \quad (11)$$

The thickness correction is defined as;

$$T \approx 0.8 + 0.7\frac{\sigma_z}{\sigma_R} \quad (12)$$

In the above equation σ_s and σ_g are the velocity dispersion of the stars and gas respectively. Q_s and Q_g are the Toomre Q of the stellar disc and gas disc respectively. A value of $Q_{RW} > 1$ indicates that the composite *stars + gas* disc is stable against axis-symmetric perturbations.

We calculate the disc dynamical stability parameter (Q) (panel 4 in Figure 18) against local, axis-symmetric perturbations of the galaxy as a function of the radius using the two-component stability parameter derived in Romeo

& Wiegert (2011). We compute the stability parameter using value of HI dispersion; $\sigma_{HI} = 5\text{km s}^{-1} 10\text{km s}^{-1} 15\text{km s}^{-1}$ in both g-band and K-band.

We find that the minimum value of Q in g-band is 1.0, 1.9, 2.5 corresponding to $\sigma_{HI} = 5\text{km s}^{-1} 10\text{km s}^{-1} 15\text{km s}^{-1}$. Similarly, in K-band the minimum value of Q is equal to 1.1 $\sigma_{HI} = 5\text{km s}^{-1} 10\text{km s}^{-1} 15\text{km s}^{-1}$. But we note that in g-band $Q > 2$ for $R < 3R_d$, indicating that the stellar disc is possibly stable, whereas in K-band the disc is closer to marinal stability. We also note that in both g-band and K-band galaxy disc is closer to marginal stability for lower values of the HI dispersion $\sigma_{HI} = 5\text{km s}^{-1}$ than for $\sigma_{HI} = 10\text{km s}^{-1}$ or $\sigma_{HI} = 15\text{km s}^{-1}$ for $R < 3R_d$. Further, we find that the value of stability parameter $Q(R < 3R_d)$ is lower than the median value of 5.5 (Aditya & Banerjee 2021) for previously studied sample of superthin galaxies and is closer to the median value of Q for calculated for a sample of spiral galaxies equal to 2.2 ± 0.6 by (Romeo & Mogotsi 2017).

– Specific angular momentum

The Fall relation (Fall & Efstathiou 1980; Romanowsky & Fall 2012; Posti et al. 2018) connects the mass to the specific angular momentum in the disc galaxies. The Fall relation is well established observationally for disc galaxies of diverse morphologies (Posti et al. 2019; Piña et al. 2021; Marasco et al. 2019), also see Kurapati et al. (2018a). The study consisting of sample of superthin galaxies and low surface brightness galaxies Jadhav Y & Banerjee (2019) showed that the specific angular momentum of the low surface brightness galaxies is higher than ordinary disc galaxies indicating that possibly high specific angular momentum drives the superthin disc stucture. We calculate $j-M$ values for FGC 1440 to see how the specific angular momentum of extremely thin disc galaxy FGC 1440 compares with a sample of previously studied superthin galaxies (Jadhav Y & Banerjee 2019) and a larger sample of disc galaxies (Piña et al. 2021). Given a rotation curve $V(R)$ and a surface density profile $\Sigma(R)$, the specific angular momentum within a radius R is given by

$$j_i(< R) = \frac{2\pi \int_0^R R'^2 \Sigma_i(R') V_i(R') dR'}{2\pi \int_0^R R' \Sigma_i(R') dR'} \quad (13)$$

In the above equation i indexes over stars(*), gas (g) and baryons (b , defined as the sum of stars and gas). We use the K-band photometry from Table. 5 for computing the j_* and M_* , and HI surface density in Figure. 4 to compute j_g and M_g . We find that

$\log_{10} \frac{j_*}{\text{kpc km s}^{-1}}$ is equal to 2.7 for the stellar mass equal to $7.9 \times 10^9 M_\odot$ and the specific angular momentum of the gas disc $\log_{10} \frac{j_g}{\text{kpc km s}^{-1}}$ is equal to 3.4 and mass of the gas disc is $1.3 \times 10^{10} M_\odot$. In Figure. 19 we compare the Fall relation for FGC 1440 (*open – points*) with other superthin galaxies (*filled – points*), the data points are taken from Jadhav Y & Banerjee (2019). We also plot the $j-M$ relation (*straight – line*) obtained for stars, gas and baryons by Piña et al. (2021) for a large sample of disc galaxies.

We find that unlike other superthin galaxies, which are outliers in the $\log_{10}(j_*) - \log_{10}(M_*)$ relation for the ordinary

disc galaxies, FGC 1440 closely follows the regression line obtained by Piña et al. (2021) in the $\log_{10}(j_*) - \log_{10}(M_*)$, $\log_{10}(j_b) - \log_{10}(M_b)$ and the $\log_{10}(j_g) - \log_{10}(M_g)$ relation.

10 CONCLUSION

We have presented the analysis and results pertaining to HI imaging of ultra-flat galaxy FGC 1440 observed using GMRT.

- We fit the busy function to the HI spectrum and find that the velocity widths 20% and the 50% of the peak maximum are 295 km s^{-1} and 306 km s^{-1} , respectively. We find that the total flux density is $10.46 \text{ Jy km s}^{-1}$.

- From our preliminary analysis of the HI data cube, we find that the moment 0 and moment 1 maps show that the HI disc is slightly warped on the north-eastern side.

- We use our final HI data to construct tilted rings model of the HI emission and derive the kinematic parameters using TiRiFic (Józsa et al. 2012) and FAT (Kamphuis et al. 2015). We find that a model with radially varying inclination equal to 90° in the inner rings and 85° for the outer rings gives a better description of the data. The best fit value of the position angle is 53.6° . We find that FGC 1440 has a slowly rising rotation curve with an asymptotic rotation velocity equal to 141.8 km s^{-1} .

- By manually comparing the PV diagrams at different offsets, we find that the HI velocity dispersion lies in between $5\text{km s}^{-1} < \sigma < 15\text{km s}^{-1}$ and the measurement of the scaleheight is limited by the resolution of the synthesized beam, $h_z < 5.3''$.

- By comparing the data with models with a varying inclination and scaleheight, we find that FGC 1440 possibly hosts a thin HI disc warped along the line of sight.

- We use the total rotation velocity along with the stellar photometry to derive the mass models in optical g-band and NIR UKIDSS K-band. We find that the mass models derived using cored pseudo-isothermal dark matter halo in conjugation with stellar rotation curves derived using Kroupa initial mass function give better fits to the observed rotation curve.

- We also derive mass models in modified Newtonian paradigm, we find that models in which both acceleration and the γ^* are kept as free parameters, the values of acceleration are lower than $1.2 \times 10^{-10} \text{ ms}^{-2}$ and the mass to light ratios tend to values maximizing the disc mass. Whereas as models in which a is fixed at $1.2 \times 10^{-10} \text{ ms}^{-2}$, γ^* tends to values predicted by stellar population synthesis models.

- Using the observed stellar scaleheight as we constrain the vertical velocity dispersion in g-band and K-band. We find that the value of central dispersion is equal to 29.0 km s^{-1} in g-Band and 18.6 km s^{-1} in K-band. We note the values of vertical dispersion are comparable to the values of dispersion quoted in Aditya & Banerjee (2021).

- Using the two-component stability parameter proposed by Romeo & Wiegert (2011), we calculate the stability factor for FGC 1440, we find that Q -value is greater than 1 for $R < 3R_d$, indicating that the galaxy is stable against axisymmetric instabilities. The value of Q for FGC 1440 is lower than the median value of Q for superthin galaxies, equal 5.5 (Aditya & Banerjee 2021) and is closer to the median value of Q for calculated for a sample of spiral galaxies equal to 2.2 ± 0.6 by (Romeo & Mogotsi 2017). We find that that

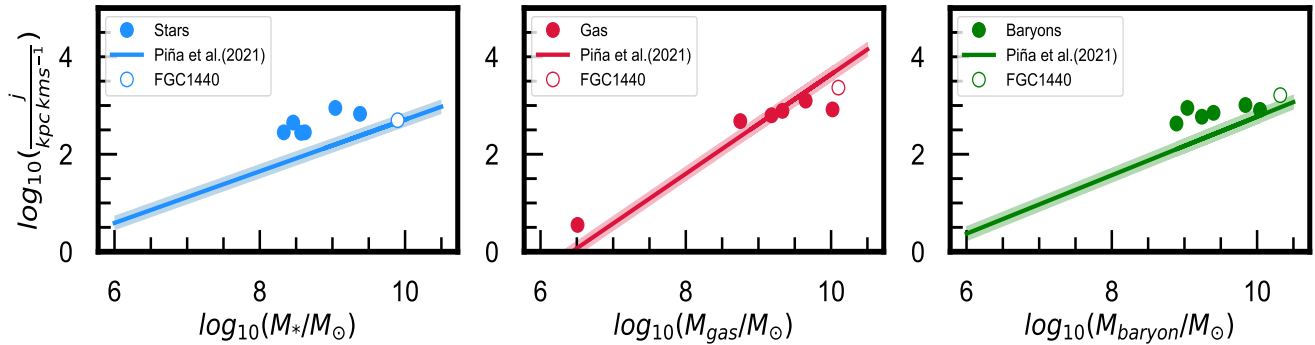


Figure 19. The plots indicate the Fall relation for superthin galaxies (filled-points) and compare it with that of FGC 1440 (open-point). The straight line shows the best-fitting Fall relation and the shaded region indicates the intrinsic scatter obtained by Piña et al. (2021) for disc galaxies.

in spite of the large axial ratios the values of $\frac{V_{Rot}}{\sigma_z} = 5$ in g-band and $\frac{V_{Rot}}{\sigma_z} = 8$ in K-band are comparable to the superthin galaxies previously studied in the literature.

- Inspecting the Fall relation, for ordinary disc galaxies, we find that FGC 1440 follows the regression line for the $\log_{10}(j_*) - \log_{10}(M_*)$, $\log_{10}(j_b) - \log_{10}(M_b)$ and $\log_{10}(j_g) - \log_{10}(M_g)$ relations. The values of j for the stars, gas and the baryons in FGC 1440 are consistent with those of normal spiral galaxies with similar mass.

11 DATA AVAILABILITY

The data from this study are available upon request.

12 ACKNOWLEDGEMENT

We thank the staff of the GMRT that made these observations possible. GMRT is run by the National Centre for Radio Astrophysics of the Tata Institute of Fundamental Research. PK is partially supported by the BMBF-project 05A17PC2 for D-MeerKAT. SB, AA, DM acknowledge the support by the Russian Science Foundation, grant 19-12-00145. We acknowledge the usage of the HyperLeda database (<http://leda.univ-lyon1.fr>). We thank Peter Yoachim for kindly providing the optical rotation curve of FGC 1440.

REFERENCES

- Abe F., et al., 1999, *The Astronomical Journal*, 118, 261
- Aditya K., Banerjee A., 2021, *Monthly Notices of the Royal Astronomical Society*, 502, 5049
- Allaert F., et al., 2015, *Astronomy & Astrophysics*, 582, A18
- Aumer M., Binney J., Schönrich R., 2016, *Monthly Notices of the Royal Astronomical Society*, 462, 1697
- Banerjee A., Bapat D., 2017, *Monthly Notices of the Royal Astronomical Society*, 466, 3753
- Banerjee A., Jog C. J., 2013, *Monthly Notices of the Royal Astronomical Society*, 431, 582
- Banerjee A., Matthews L. D., Jog C. J., 2010, *New Astronomy*, 15, 89
- Banerjee A., Patra N. N., Chengalur J. N., Begum A., 2013, *Monthly Notices of the Royal Astronomical Society*, 434, 1257
- Barrera-Ballesteros J., et al., 2021, arXiv preprint arXiv:2101.04683
- Begeman K., Broeils A., Sanders R., 1991, *Monthly Notices of the Royal Astronomical Society*, 249, 523
- Bell E. F., de Jong R. S., 2001, *The Astrophysical Journal*, 550, 212
- Bell E. F., McIntosh D. H., Katz N., Weinberg M. D., 2003, *The Astrophysical Journal Supplement Series*, 149, 289
- Bertin E., Arnouts S., 1996, *Astronomy and astrophysics supplement series*, 117, 393
- Bigieli F., Leroy A., Walter F., Brinks E., De Blok W., Madore B., Thornley M. D., 2008, *The Astronomical Journal*, 136, 2846
- Bolatto A. D., et al., 2017, *The Astrophysical Journal*, 846, 159
- Bothun G., Impey C., McGaugh S., 1997, *Publications of the Astronomical Society of the Pacific*, 109, 745
- Bottama R., Pestana J. L. G., 2015, *Monthly Notices of the Royal Astronomical Society*, 448, 2566
- Byun Y.-I., 1998, *Chinese Journal of Physics*, 36, 677
- Chan M. H., Hui H. K., 2018, *The Astrophysical Journal*, 856, 177
- Courteau S., 1997, *The Astronomical Journal*, 114, 2402
- Dalcanton J. J., Bernstein R. A., 2000, *The Astronomical Journal*, 120, 203
- Dalcanton J. J., Bernstein R. A., 2002, *The Astronomical Journal*, 124, 1328
- Dalcanton J. J., Shectman S. A., 1996, *The Astrophysical Journal Letters*, 465, L9
- Dalcanton J. J., Yoachim P., Bernstein R. A., 2004, *The Astrophysical Journal*, 608, 189
- De Blok W., McGaugh S. S., Rubin V. C., 2001a, *The Astronomical Journal*, 122, 2396
- De Blok W., McGaugh S. S., Bosma A., Rubin V. C., 2001b, *The Astrophysical Journal Letters*, 552, L23
- De Blok W., Walter F., Brinks E., Trachternach C., Oh S., Kenicutt Jr R., 2008, *The Astronomical Journal*, 136, 2648
- De Naray R. K., McGaugh S. S., De Blok W., 2008, *The Astrophysical Journal*, 676, 920
- De Vaucouleurs G., De Vaucouleurs A., Corwin J., Buta R., Paturel G., Fouque P., 1991, *Third Reference Catalogue of Bright Galaxies, Version 3.9*. Springer, New York, NY
- Donato F., Gentile G., Salucci P., 2004, *Monthly Notices of the Royal Astronomical Society*, 353, L17
- Dutton A. A., Maccio A. V., 2014, *Monthly Notices of the Royal Astronomical Society*, 441, 3359

- Fall S. M., Efstathiou G., 1980, *Monthly Notices of the Royal Astronomical Society*, 193, 189
- Fuchs B., Möllenhoff C., Heidt J., 1998, arXiv preprint astro-ph/9806117
- Gallagher J., Hudson H., 1976, *The Astrophysical Journal*, 209, 389
- Garg P., Banerjee A., 2017, *Monthly Notices of the Royal Astronomical Society*, 472, 166
- Gentile G., Famaey B., de Blok W., 2011, *Astronomy & Astrophysics*, 527, A76
- Gentile G., et al., 2013, *Astronomy & Astrophysics*, 554, A125
- Ghari A., Famaey B., Laporte C., Haghi H., 2019, *Astronomy & Astrophysics*, 623, A123
- Ghosh S., Jog C. J., 2014, *Monthly Notices of the Royal Astronomical Society*, 439, 929
- Goad J., Roberts M., 1981, *The Astrophysical Journal*, 250, 79
- Grand R. J., et al., 2016, *Monthly Notices of the Royal Astronomical Society: Letters*, 460, L94
- Haynes M. P., et al., 2018, *The Astrophysical Journal*, 861, 49
- Heald G., et al., 2011, *Astronomy & Astrophysics*, 526, A118
- Hoffman G. L., Williams B., Lewis B., Helou G., Salpeter E., 1989, *The Astrophysical Journal Supplement Series*, 69, 65
- Hunter D. A., et al., 2012, *The Astronomical Journal*, 144, 134
- Jadhav Y. V., Banerjee A., 2019, *Monthly Notices of the Royal Astronomical Society*, 488, 547
- Jenkins A., Binney J., 1990, *Monthly Notices of the Royal Astronomical Society*, 245, 305
- Jog C. J., 1996, *Monthly Notices of the Royal Astronomical Society*, 278, 209
- Józsa G. I., Kenn F., Oosterloo T. A., Klein U., 2012, *ascl*, pp ascl-1208
- Kamphuis P., 2008, *The structure and kinematics of halos in disk galaxies. University Library Groningen*[Host]
- Kamphuis P., et al., 2013, *Monthly Notices of the Royal Astronomical Society*, 434, 2069
- Kamphuis P., Józsa G., Oh S.-H., Spekkens K., Urbancic N., Serra P., Koribalski B., Dettmar R.-J., 2015, *ascl*, pp ascl-1507
- Karachentsev I., Karachentseva V., Parnovsky S., 1993, *Astronomische Nachrichten*, 314, 97
- Karachentsev I., Karachentseva V., Kudrya Y. N., Sharina M., Parnovsky S., 2003, arXiv preprint astro-ph/0305566
- Karachentseva V., Kudrya Y. N., Karachentsev I., Makarov D., Mehnyk O., 2016, *Astrophysical Bulletin*, 71, 1
- Kautsch S. J., 2009, *Publications of the Astronomical Society of the Pacific*, 121, 1297
- Keller B., Wadsley J., 2017, *The Astrophysical Journal Letters*, 835, L17
- Komanduri A., Banerjee I., Banerjee A., Sengupta S., 2020, *Monthly Notices of the Royal Astronomical Society*, 499, 5690
- Kourkchi E., Courtois H. M., Graziani R., Hoffman Y., Pomarède D., Shaya E. J., Tully R. B., 2020, *The Astronomical Journal*, 159, 67
- Kregel M., Van Der Kruit P., Freeman K., 2005, *Monthly Notices of the Royal Astronomical Society*, 358, 503
- Kroupa P., 2001, *Monthly Notices of the Royal Astronomical Society*, 322, 231
- Kurapati S., Chengalur J. N., Pustilnik S., Kamphuis P., 2018a, *Monthly Notices of the Royal Astronomical Society*, 479, 228
- Kurapati S., Banerjee A., Chengalur J. N., Makarov D., Borisov S., Afanasiev A., Antipova A., 2018b, *Monthly Notices of the Royal Astronomical Society*, 479, 5686
- Lelli F., McGaugh S. S., Schombert J. M., 2016, *The Astronomical Journal*, 152, 157
- Leroy A. K., Walter F., Brinks E., Bigiel F., De Blok W., Madore B., Thornley M., 2008, *The astronomical journal*, 136, 2782
- Li P., Lelli F., McGaugh S., Schombert J., 2018, *Astronomy & Astrophysics*, 615, A3
- Li P., Lelli F., McGaugh S. S., Starkman N., Schombert J. M., 2019, *Monthly Notices of the Royal Astronomical Society*, 482, 5106
- Makarov D., Prugniel P., Terekhova N., Courtois H., Vauglin I., 2014, *Astronomy & Astrophysics*, 570, A13
- Marasco A., Fraternali F., Posti L., Ijtsma M., Di Teodoro E., Oosterloo T., 2019, *Astronomy & Astrophysics*, 621, L6
- Matthews L. D., Uson J. M., 2007, *The Astronomical Journal*, 135, 291
- Matthews L., Uson J. M., 2008, *The Astrophysical Journal*, 688, 237
- Matthews L. D., Wood K., 2003, *The Astrophysical Journal*, 593, 721
- Matthews L., Gallagher III J., Van Driel W., 1999, *The Astronomical Journal*, 118, 2751
- McGaugh S. S., 1996, *Monthly Notices of the Royal Astronomical Society*, 280, 337
- McGaugh S. S., Rubin V. C., De Blok W., 2001, *The Astronomical Journal*, 122, 2381
- McMullin J. P., Waters B., Schiebel D., Young W., Golap K., 2007, in *Astronomical data analysis software and systems XVI*. p. 127
- Milgrom M., 1983, *The Astrophysical Journal*, 270, 371
- Naik A. P., Puchwein E., Davis A.-C., Sijacki D., Desmond H., 2019, *Monthly Notices of the Royal Astronomical Society*, 489, 771
- Narayan C. A., Jog C. J., 2002, *Astronomy & Astrophysics*, 394, 89
- Narayanan G., Banerjee A., 2021, arXiv preprint arXiv:2104.04216
- Navarro J. F., Frenk C. S., White S. D., 1997, *The Astrophysical Journal*, 490, 493
- Newville M., Stensitzki T., Allen D. B., Rawlik M., Ingargiola A., Nelson A., 2016, *Astrophysics Source Code Library*, pp ascl-1606
- O'Brien J. C., Freeman K., van der Kruit P., 2010, *Astronomy & Astrophysics*, 515, A62
- Oh S.-H., et al., 2015, *The Astronomical Journal*, 149, 180
- Olling R. P., 1995, arXiv preprint astro-ph/9505002
- Olling R. P., 1996, arXiv preprint astro-ph/9605111
- Patra N. N., 2018, *Monthly Notices of the Royal Astronomical Society*, 478, 4931
- Patra N. N., 2020a, *Monthly Notices of the Royal Astronomical Society*, 499, 2063
- Patra N. N., 2020b, *Astronomy & Astrophysics*, 638, A66
- Patra N. N., Jog C. J., 2019, *Monthly Notices of the Royal Astronomical Society*, 488, 4942
- Peng C. Y., Ho L. C., Impey C. D., Rix H.-W., 2011, *Astrophysics Source Code Library*, pp ascl-1104
- Peters S., van der Kruit P., Allen R., Freeman K., 2017, *Monthly Notices of the Royal Astronomical Society*, 464, 65
- Phookun B., Vogel S. N., Mundy L. G., 1993, *The Astrophysical Journal*, 418, 113
- Piña P. E. M., Posti L., Fraternali F., Adams E. A., Oosterloo T., 2021, *Astronomy & Astrophysics*, 647, A76
- Pohlen M., Balcells M., Lütticke R., Dettmar R.-J., 2003, *Astronomy & Astrophysics*, 409, 485
- Posti L., Fraternali F., Di Teodoro E. M., Pezzulli G., 2018, *Astronomy & Astrophysics*, 612, L6
- Posti L., Marasco A., Fraternali F., Famaey B., 2019, *Astronomy & Astrophysics*, 629, A59
- Punzo D., 2017, PhD thesis, Rijksuniversiteit Groningen
- Romanowsky A. J., Fall S. M., 2012, *The Astrophysical Journal Supplement Series*, 203, 17
- Romeo A. B., Falstad N., 2013, *Monthly Notices of the Royal Astronomical Society*, 433, 1389
- Romeo A. B., Mogotsi K. M., 2017, *Monthly Notices of the Royal Astronomical Society*, 469, 286
- Romeo A. B., Wiegert J., 2011, *Monthly Notices of the Royal*

- Astronomical Society, 416, 1191
- Rubin V. C., Ford Jr W. K., Thonnard N., 1980, *The Astrophysical Journal*, 238, 471
- Rubin V. C., Burstein D., Ford Jr W. K., Thonnard N., 1985, *The Astrophysical Journal*, 289, 81
- Saha K., 2014, arXiv preprint arXiv:1403.1711
- Sarkar S., Jog C. J., 2019a, arXiv preprint arXiv:1905.02735
- Sarkar S., Jog C. J., 2019b, *Proceedings of the International Astronomical Union*, 14, 13
- Sarkar S., Jog C. J., 2020, *Monthly Notices of the Royal Astronomical Society*, 492, 628
- Serra P., et al., 2015, *Monthly Notices of the Royal Astronomical Society*, 448, 1922
- Toomre A., 1964, *The Astrophysical Journal*, 139, 1217
- Uson J. M., Matthews L., 2003, *The Astronomical Journal*, 125, 2455
- Van der Hulst J., Terlouw J., Begeman K., Zwitter W., Roelfsema P., 1992, in *Astronomical Data Analysis Software and Systems I*. p. 131
- Virtanen P., et al., 2020, *Nature methods*, 17, 261
- Voigtländer P., Kamphuis P., Marcelin M., Bomans D. J., Dettmar R.-J., 2013, *Astronomy & Astrophysics*, 554, A133
- Vorontsov-Vel'yaminov B., 1974, *Soviet Astronomy*, 17, 452
- Walter F., Brinks E., De Blok W., Bigiel F., Kennicutt Jr R. C., Thornley M. D., Leroy A., 2008, *The Astronomical Journal*, 136, 2563
- Westmeier T., Jurek R., Obreschkow D., Koribalski B. S., Staveley-Smith L., 2014, *Monthly Notices of the Royal Astronomical Society*, 438, 1176
- Wyder T., et al., 2009, *The Galaxy Disk in Cosmological Context*, 254, 77
- Yoachim P., Dalcanton J. J., 2005, *The Astrophysical Journal*, 624, 701
- Yoachim P., Dalcanton J. J., 2008, *The Astrophysical Journal*, 682, 1004
- Yock P., Pennycook G., Rattenbury N., Koribalski B., Muraki Y., Yanagisawa T., Jugaku J., Dodd R., 1999, in *The Third Stromlo Symposium: The Galactic Halo*. p. 187
- Zschaechner L. K., Rand R. J., Heald G. H., Gentile G., Józsa G., 2012, *The Astrophysical Journal*, 760, 37
- van der Kruit P., Jiménez-Vicente J., Kregel M., Freeman K., 2001, *Astronomy & Astrophysics*, 379, 374

13 APPENDIX-A**14 APPENDIX-B**

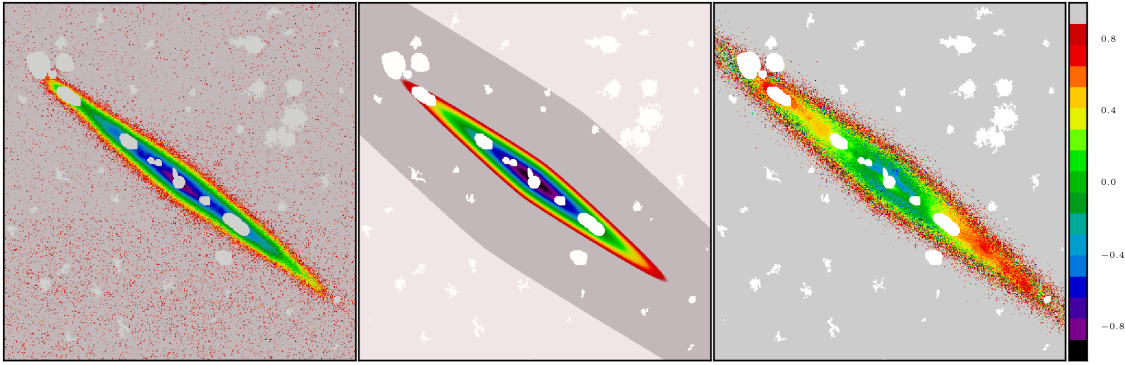


Figure 20. The image shows the data (panel 1), the Galfit model (panel 2) and the normalized difference between the data and the model (panel 3) for optical photometry of FGC 1440 using the SDSS g-band image.

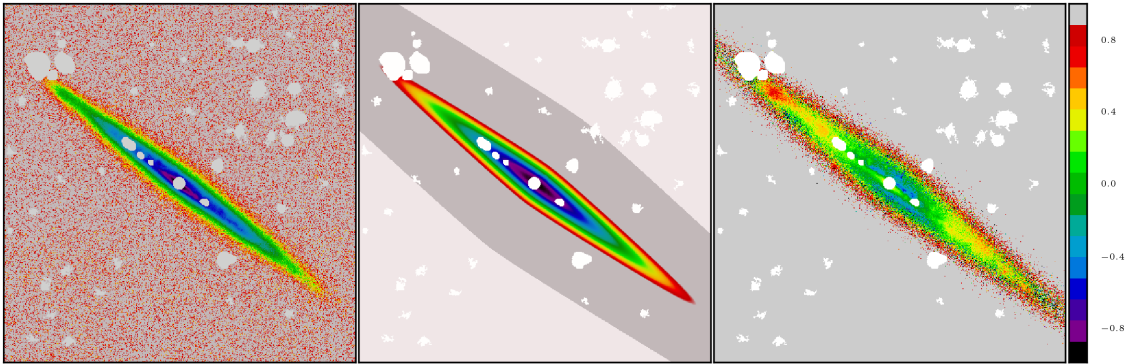


Figure 21. The image shows the data (panel 1), the Galfit model (panel 2) and the normalized difference between the data and the model (panel 3) for optical photometry of FGC 1440 using the SDSS r-band image.

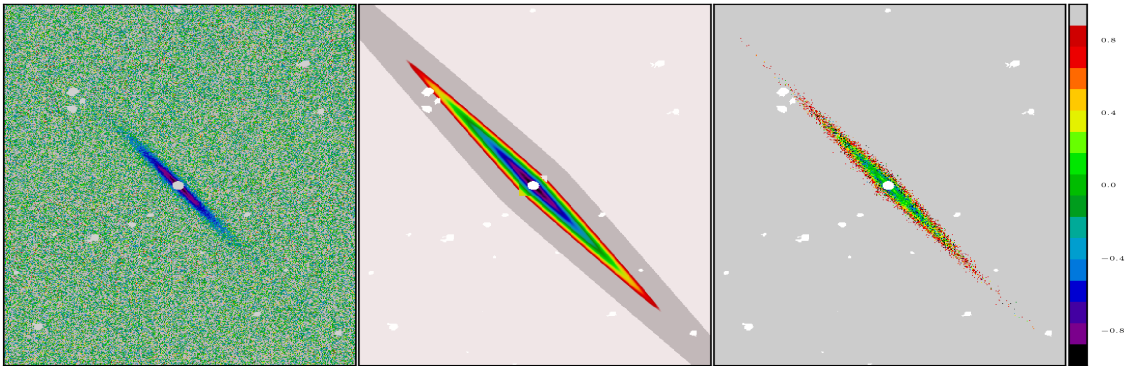


Figure 22. The image shows the data (panel 1), the Galfit model (panel 2) and the normalized difference between the data and the model (panel 3) for optical photometry of FGC 1440 using the UKIDSS K-band image.

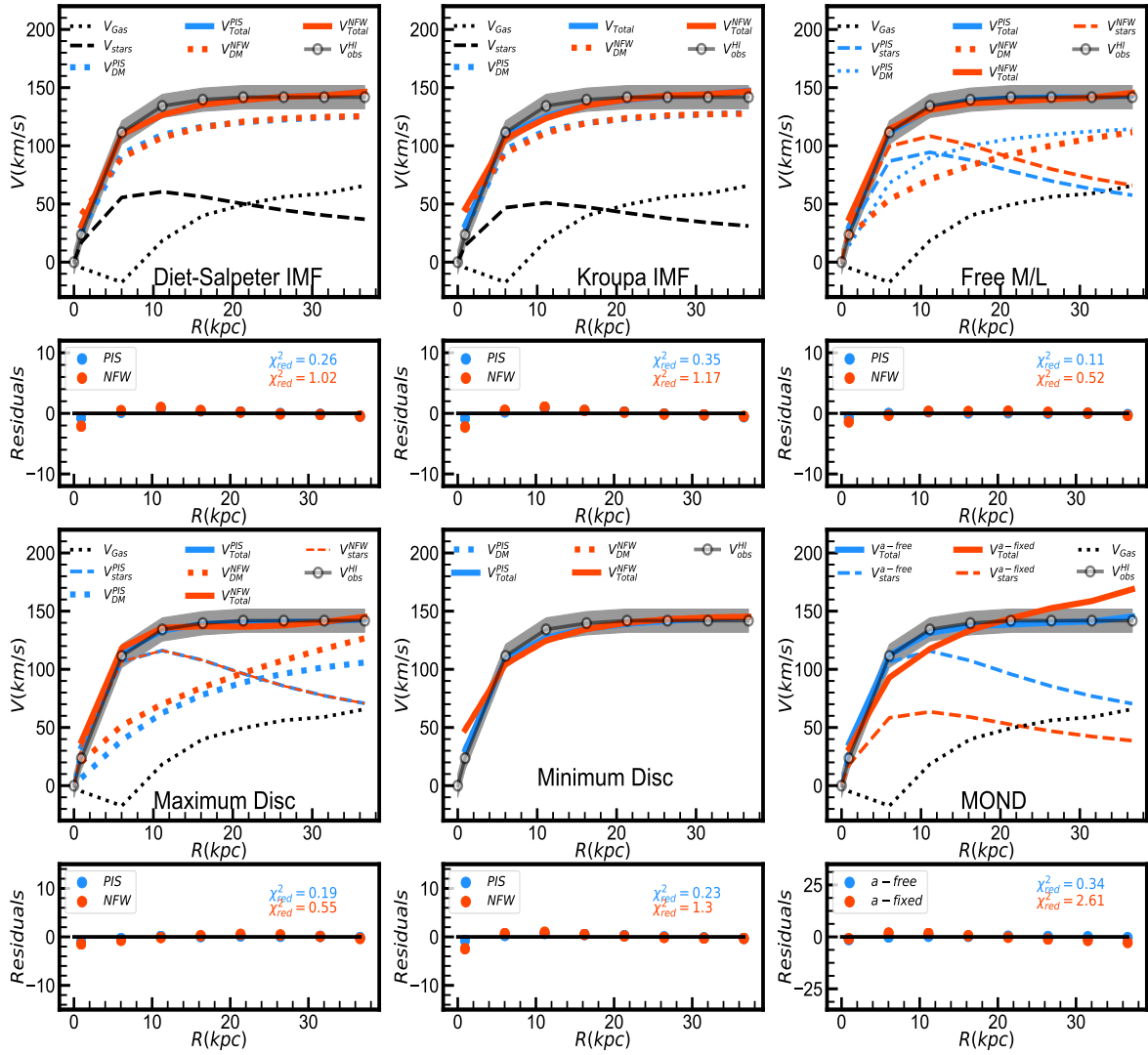


Figure 23. We present the mass-model of the galaxy FGC 1440 derived using SDSS g-band photometry. The mass models are constrained using the HI 21 cm data.

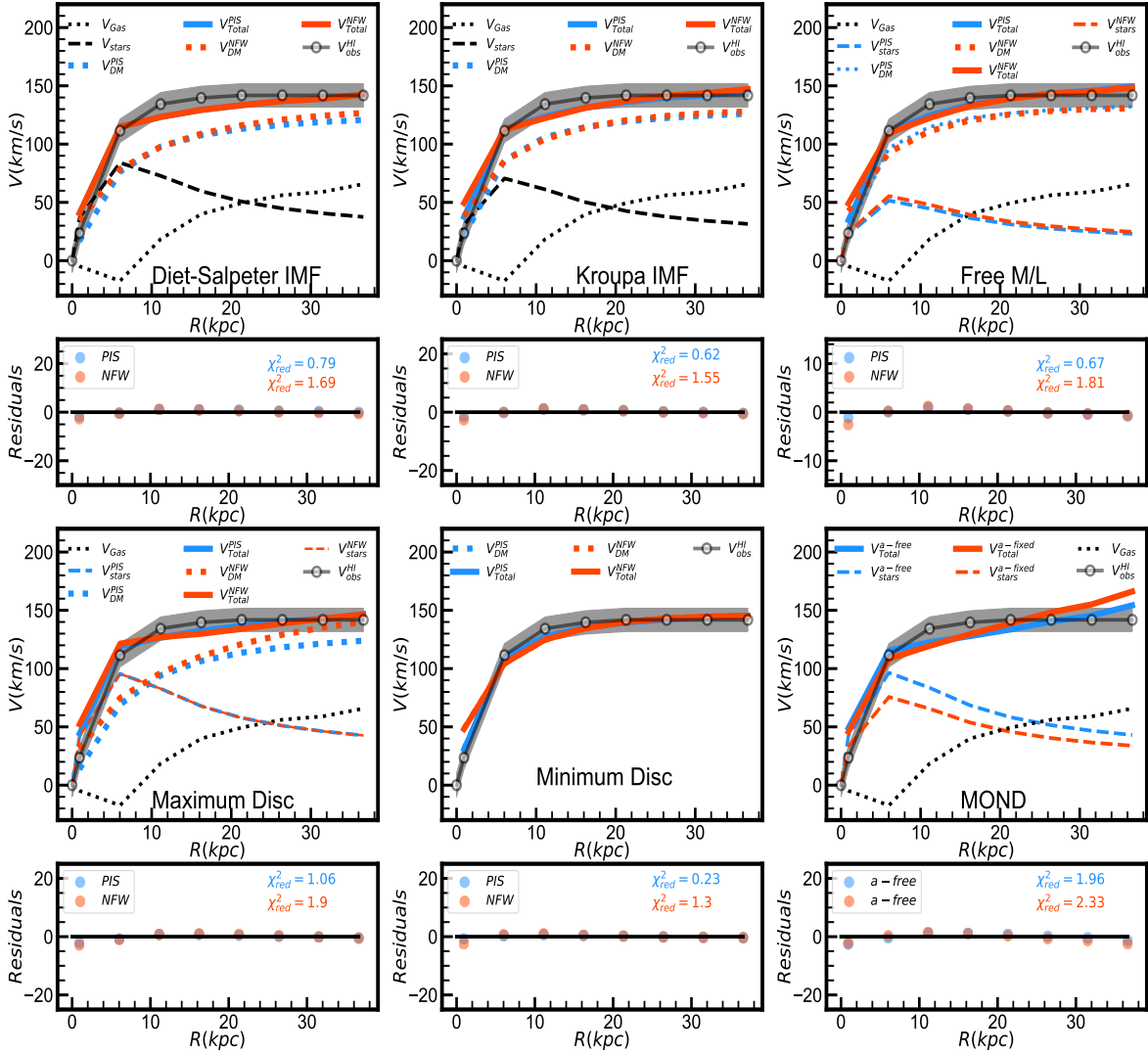


Figure 24. We present the mass-model of the galaxy FGC 1440 derived using UKIDSS K-band photometry. The mass models are constrained using the HI 21 cm data.

Table 9. Dark matter density parameters derived from mass-modeling using the optical g-band and NIR K band photometry using just the HI rotation curve.

Model	$c^{(a)}$	$R_{200}^{(b)}$ (kpc)	$\gamma^{*(c)}$	$\frac{V_{max}}{V_{200}}^{(d)}$	$\chi_{red}^{2(e)}$	$\rho_0^{(f)} \times 10^{-3}$ M_{\odot}/pc^3	$R_c^{(g)}$ (kpc)	$\gamma^{*(h)}$	$\frac{R_c}{R_d}^{(i)}$	$\chi_{red}^{2(j)}$
g-band	NFW profile					PIS profile				
'diet' Salpeter	4.65 ± 1.18	87.15 ± 7.2	3.8	2.23	1.02	45.92 ± 12.7	2.66 ± 0.42	3.8	0.60	0.26
Kroupa IMF	5.10 ± 1.27	87.4 ± 7.07	2.6	2.22	1.17	54.78 ± 16.4	2.48 ± 0.42	2.6	0.56	0.35
Free γ^*	1.06 ± 1.43	103.5 ± 35.8	12.19 ± 2.84	1.87	0.52	13.08 ± 8.65	4.76 ± 1.60	9.26 ± 2.10	1.07	0.11
Maximum Disc	0.05 ± 0.74	221.36 ± 179.9	14	0.87	0.55	2.7 ± 0.86	11.19 ± 2.7	14	2.53	0.19
Minimum Disc	5.4 ± 1.16	98.7 ± 7.23	0	1.97	1.3	65.81 ± 13.04	2.56 ± 0.29	0	0.57	0.23
K-Band										
'diet' Salpeter	3.13 ± 1.3	94.3 ± 13.95	0.85	2.06	1.69	18.69 ± 8.63	4.15 ± 1.22	0.85	1.60	0.79
Kroupa IMF	3.94 ± 1.32	91.38 ± 10.51	0.6	2.12	1.55	29.035 ± 11.81	3.42 ± 0.84	0.6	1.3	0.62
Free γ^*	4.72 ± 2.73	90.71 ± 10.37	0.37 ± 0.63	2.14	1.81	46.7 ± 34.2	2.79 ± 1.04	0.32 ± 0.36	1.08	0.67
Maximum Disc	2.10 ± 1.14	117.56 ± 26.3	1.1	1.65	1.9	12.16 ± 6.46	5.43 ± 1.83	1.1	2.10	1.06
Minimum Disc	5.41 ± 1.61	98.7 ± 7.23	0	1.97	1.3	65.81 ± 13.04	2.57 ± 0.29	0	0.99	0.23
MOND										
	$a^{(k)}$ $m^2 s^{-2}$	$\gamma^{*(l)}$	$\chi_{red}^{2(m)}$							
g-Band	0.4×10^{-10}	13.89 ± 1.64	0.34							
<i>g - Band</i> ^{a=fixed}	1.2×10^{-10}	2.61								
K-Band	0.8×10^{-10}	1.12 ± 0.4	1.96							
<i>K - Band</i> ^{a=fixed}	1.2×10^{-10}	0.69 ± 0.18	2.33							

(a): Concentration parameter of the NFW profile

(b): Radius at which the mean density equal 200 times the critical density.

(c): Mass to light ratio derived using population synthesis models or estimated as a free parameter.

(d): Ratio of the asymptotic velocity to the velocity at R_{200} , where $\frac{V_{200}}{\text{km s}^{-1}} = 0.73 \frac{R_{200}}{\text{kpc}}$ (Navarro et al. 1997)

(e): Reduced chi-square value corresponding to the fit.

(f): The central dark matter density of the PIS dark matter halo model

(g): The core radius of the PIS dark matter halo model

(h): Mass to light ratio derived using population synthesis models or estimated as a free parameter.

(i): Ratio of the core radius and the disk scalelength.

(j): Reduced chi square value corresponding to the fit.

(k): Acceleration per length in MOND.

(l): Estimated Mass to light ratio in MOND.

(m): Reduced chi square corresponding to the fit.